



<b>Publication Year</b>	2015
<b>Acceptance in OA</b>	2020-04-21T11:02:30Z
<b>Title</b>	Asymptotic giant branch stars in the Large Magellanic Cloud: evolution of dust in circumstellar envelopes
<b>Authors</b>	Dell'Agli, F., VENTURA, Paolo, SCHNEIDER, RAFFAELLA, DI CRISCIENZO, Marcella, García-Hernández, D. A., Rossi, C., BROCATO, Enzo
<b>Publisher's version (DOI)</b>	10.1093/mnras/stu2559
<b>Handle</b>	<a href="http://hdl.handle.net/20.500.12386/24157">http://hdl.handle.net/20.500.12386/24157</a>
<b>Journal</b>	MONTHLY NOTICES OF THE ROYAL ASTRONOMICAL SOCIETY
<b>Volume</b>	447

# Asymptotic giant branch stars in the Large Magellanic Cloud: evolution of dust in circumstellar envelopes

F. Dell’Agli,<sup>1,2</sup> P. Ventura,<sup>2\*</sup> R. Schneider,<sup>2</sup> M. Di Criscienzo,<sup>2</sup>  
D. A. García-Hernández,<sup>3,4</sup> C. Rossi<sup>1</sup> and E. Brocato<sup>2</sup>

<sup>1</sup>Dipartimento di Fisica, Università di Roma ‘La Sapienza’, P. le Aldo Moro 5, I-00143 Roma, Italy

<sup>2</sup>INAF – Osservatorio Astronomico di Roma, Via Frascati 33, I-00040 Monte Porzio Catone (RM), Italy

<sup>3</sup>Instituto de Astrofísica de Canarias, E-38200 La Laguna, Tenerife, Spain

<sup>4</sup>Departamento de Astrofísica, Universidad de La Laguna (ULL), E-38206 La Laguna, Tenerife, Spain

Accepted 2014 December 2. Received 2014 November 11; in original form 2014 August 20

## ABSTRACT

We calculated theoretical evolutionary sequences of asymptotic giant branch (AGB) stars, including the formation and evolution of dust grains in their circumstellar envelopes. By considering stellar populations of the Large Magellanic Cloud (LMC), we calculate synthetic colour–colour and colour–magnitude diagrams, which are compared with those obtained by the *Spitzer* Space Telescope. The comparison between observations and theoretical predictions outlines that extremely obscured carbon stars and oxygen-rich sources experiencing hot bottom burning (HBB) occupy well-defined, distinct regions in the colour–colour ([3.6] – [4.5], [5.8] – [8.0]) diagram. The C-rich stars are distributed along a diagonal strip that we interpret as an evolutionary sequence, becoming progressively more obscured as the stellar surface layers enrich in carbon. Their circumstellar envelopes host solid carbon dust grains with size in the range  $0.05 < a < 0.2 \mu\text{m}$ . The presence of silicon carbide (SiC) particles is expected only in the more metal-rich stars. The reddest sources, with  $[3.6] - [4.5] > 2$ , are the descendants of stars with initial mass  $M_{\text{in}} \sim 2.5\text{--}3 M_{\odot}$  in the very latest phases of AGB life. The oxygen-rich stars with the reddest colours ( $[5.8] - [8.0] > 0.6$ ) are those experiencing HBB, the descendants of  $\sim 5 M_{\odot}$  objects formed  $10^8$  yr ago; alumina and silicate dust starts forming at different distances from the central star. The overall dust production rate in the LMC is  $\sim 4.5 \times 10^{-5} M_{\odot} \text{yr}^{-1}$ , the relative percentages due to C and M stars being 85 and 15 per cent, respectively.

**Key words:** stars: abundances – stars: AGB and post-AGB – ISM: abundances – dust, extinction – Magellanic Clouds.

## 1 INTRODUCTION

The stellar sources most relevant for dust production are low- and intermediate-mass stars during the asymptotic giant branch (AGB) phase and supernovae (SNe). A full understanding of the amount of dust produced by these stellar sources is essential to account for the presence of a large quantity of dust in galaxies. The analysis of the spectral energy distribution (SED) of high-redshift quasars shows that large reservoirs of dust are observed up to redshift  $z \sim 6.4$  (Bertoldi et al. 2003; Priddey et al. 2003; Robson et al. 2004; Beelen et al. 2006; Wang et al. 2008, 2013). Several investigations have addressed dust evolution in galaxies of the Local Group (Dwek 1998; Calura, Pipino & Matteucci 2008; Zhukovska, Gail & Tieloff 2008; Boyer 2013; De Bressan et al. 2014; Schneider et al. 2014) and in high-redshift galaxies (Morgan & Edmunds 2003; Calura et al.

2008). These works were aimed not only at providing an exhaustive explanation of the observational scenario but also at explaining the presence of dust at early epochs (Valiante et al. 2009, 2011; Dwek & Cherchneff 2011; Mattson 2011; Pipino et al. 2011). Concerning high redshifts, a lively debate is still open regarding the dominant source of dust. Early investigations suggested the dominant role of SNe (Maiolino et al. 2004), a conclusion challenged by subsequent studies that stressed the importance of dust destruction by SNe reverse shocks (Nozawa, Kozasa & Habe 2006; Bianchi & Schneider 2007; Silvia, Smith & Shull 2010, 2012). Recent studies showed that the dust present at high redshifts is produced by all stars more massive than  $\sim 3 M_{\odot}$ , which points in favour of a non-negligible contribution from the AGB (Valiante et al. 2009).

Study of the dust produced by AGB stars has been proved to be extremely useful in several astrophysical contexts, given the central role played by these stars in dust production and evolution in galaxies. The pioneering investigations by the Heidelberg group (Gail & Sedlmayr 1985, 1999; Ferrarotti & Gail 2006; Zhukovska

\* E-mail: paolo.ventura@oa-roma.inaf.it

et al. 2008) were the first attempts to track down the dust condensation sequences in AGB stars numerically: their scheme is based on a basic description of the stellar wind, assumed to expand isotropically from the stellar surface and accelerated by radiation pressure acting on the dust grains. This approach represents an extremely simplified schematization of a more complex situation, where formation and growth of dust particles is likely favoured by periodic shocks, triggered by large-amplitude pulsations experienced by AGBs (Wood 1979; Bertschinger & Chevalier 1985; Bowen 1988; Fleischer, Gauger & Sedlmayr 1992). However, the hydrostatic atmosphere approximation is currently the only description that can be easily interfaced with stellar evolution codes and it was adopted more recently by different groups involved in this research (Ventura et al. 2012a,b, 2014a; Di Criscienzo et al. 2013; Nanni et al. 2013a,b, 2014). The results are still far from being completely reliable, owing to the uncertainties affecting the AGB evolution (mainly the description of mass loss and the treatment of convective instability) and the dust formation process (e.g. sticking coefficients of some species, extinction properties, etc.). The differences among the results presented by the various groups outline the need for a further refinement of the models (Nanni et al. 2013b; Ventura et al. 2014a).

Comparison with the observational scenario is therefore mandatory to confirm or disregard the theoretical models produced so far. The analysis of dusty AGBs in the Galaxy is not straightforward, owing to obscuration from its own interstellar medium and the unknown distances, which render uncertain the luminosity of the sources observed. The Large Magellanic Cloud (LMC) is a much more favourable target, as it is relatively close (50 kpc: Feast 1999) and with a low average reddening ( $E(B - V) \sim 0.075$ : Schlegel, Finkbeiner & Davis 1998). A growing body of observational data, based on dedicated photometric surveys, has been made available to the community: the Magellanic Clouds Photometric Survey (MCPS: Zaritsky et al. 2004), the Two-Micron All Sky Survey (2MASS: Skrutskie et al. 2006), the Deep Near Infrared Survey of the Southern Sky (DENIS: Epchtein et al. 1994), Surveying the Agents of a Galaxy's Evolution Survey (SAGE-LMC with the *Spitzer* Space Telescope: Meixner et al. 2006) and the *HERschel* Inventory of the Agents of Galaxy Evolution (HERITAGE: Meixner et al. 2010, 2013).

Additional data allowed us to reconstruct the star formation history (SFH) of the LMC (Harris & Zaritsky 2009; Weisz et al. 2013) and the age–metallicity relation (AMR: Carrera et al. 2008; Piatti & Geisler 2013). These results, in combination with the models of dust production by AGBs currently available, were used to determine the dust production rates of AGB stars, for comparison with observations of evolved stars in the LMC (Zhukovska & Henning 2013; Schneider et al. 2014).

The large amount of data available, particularly in the infrared bands, where most of the emission from dust-enshrouded stars occurs, stimulated a series of investigations, with the scope of interpreting the observed colour–colour and colour–magnitude diagrams, based on reprocessing of the radiation emitted from the central star by dust particles present in the circumstellar envelope (Srinivasan et al. 2009; Boyer et al. 2011; Sargent, Srinivasan & Meixner 2011; Srinivasan, Sargent & Meixner 2011). These works are based on a wide exploration of the various quantities relevant for the determination of the spectrum of a single object (effective temperature, surface gravity, luminosity, optical depth, size of the individual dust species formed), in an attempt to select the combinations of parameters allowing the best agreement with the observations and to refine further the suggested classification of

dust-obscured stars in the LMC (Cioni et al. 2006; Blum et al. 2006).

In the present work, we tackle this problem from a different point of view. Our goal is to provide a full and exhaustive interpretation of the observed distribution of dust-obscured AGB stars in the LMC, in the various colour–colour and colour–magnitude diagrams (CCD and CMD, respectively) obtained with the *Spitzer* Space Telescope bands. In particular, we use the bands of the InfraRed Array Camera (IRAC: 3.6, 4.5, 5.8 and 8.0  $\mu\text{m}$ ) and the 24- $\mu\text{m}$  band of the Multi-band Imaging Photometer (MIPS). This choice allows a detailed analysis of the properties of the individual star+dusty envelope systems, the spectral energy distributions (SEDs) of which peak in the infrared.

Our theoretical description is based on a complete modelling of the AGB phase, which also accounts for dust formation in the wind, published in Ventura et al. (2012a,b, 2014a).

This work represents an important step forward compared with the previously mentioned investigations, for the following reasons: (i) the choice of parameters relevant to the determination of the synthetic spectra is not free, but rather is based on the results coming from AGB modelling; (ii) the mass distribution of the stars is calculated based on the LMC SFH by Harris & Zaritsky (2009), according to the evolutionary times of the individual stars; (iii) we do not use a single metallicity, but rather account for the distribution among different chemistries given by Harris & Zaritsky (2009), considering models with  $Z = 10^{-3}$ ,  $Z = 4 \times 10^{-3}$ ,  $Z = 8 \times 10^{-3}$ ; (iv) points (ii) and (iii) allow not only a qualitative comparison between the observed colours of individual stars and the expectations from evolutionary tracks, but also a quantitative, statistical analysis, based on the relative number of stars populating different zones of the CCD and CMD considered.

A first step in this direction was recently made by Dell'Agli et al. (2014a), who analysed the group of dust-obscured stars in the LMC classified as ‘extreme’ (Blum et al. 2006); following Srinivasan et al. (2011), they interpreted their distribution in the colour–colour ([3.6] – [4.5], [5.8] – [8.0]) diagram using  $Z = 8 \times 10^{-3}$  models of AGB evolution + dust production in the winds. Here we extend this work further, by considering a much larger sample of over 6000 AGB candidates and adopting the appropriate metallicity distribution suggested by Harris & Zaritsky (2009).

The present investigation proves important not only for interpreting the properties of AGB stars in the LMC; it also constitutes an important test for AGB modelling and for the description of the dust formation process in the winds of AGBs.

The article is organized as follows: Section 2 gives the numerical and physical input adopted to build the evolutionary sequences and to describe dust formation in the winds; an overview of the main evolutionary properties of AGBs is given in Section 3; we propose a classification of AGBs based on their position in the colour–colour and colour–magnitude diagrams obtained with the *Spitzer* filters in Section 4. Section 5 presents an overview of the observations of dust-obscured AGBs in the LMC and the synthetic modelling used for population synthesis. Interpretation of the data is addressed in Section 6, while in Section 7 we suggest the evolutionary status of the stars in pre-existing classifications. Section 8 is focused on the expected dust production rate by AGBs. Our conclusions are given in Section 9.

## 2 NUMERICAL AND PHYSICAL INPUTS

To produce synthetic diagrams for comparison with the observed distribution of LMC AGB stars in the different colour–colour and

**Table 1.** Time-scales of stars of intermediate mass of different metallicity in terms of the duration of the core hydrogen-burning phase ( $\tau_{\text{ev}}$ ) and the whole AGB phase ( $\tau_{\text{AGB}}$ ). The latter time-scale was determined by considering the time elapsed from the phase following the exhaustion of central helium to the total loss of the external mantle.

$M/M_{\odot}$	$\tau_{\text{ev}}$ (Myr) $Z = 10^{-3}$	$\tau_{\text{AGB}}$ (kyr)	$\tau_{\text{ev}}$ (Myr) $Z = 4 \times 10^{-3}$	$\tau_{\text{AGB}}$ (kyr)	$\tau_{\text{ev}}$ (Myr) $Z = 8 \times 10^{-3}$	$\tau_{\text{AGB}}$ (kyr)
1.00	5400	1600	5700	1160	8020	1500
1.25	2500	1520	2690	1240	3270	1520
1.50	1480	1520	1630	1760	1890	1510
2.00	700	2000	768	4480	888	1500
2.50	410	880	566	1570	690	3000
3.00	279	450	282	611	413	990
3.50	196	360	235	315	268	450
4.00	146	280	170	237	190	290
4.50	130	200	130	197	141	210
5.00	92	140	102	152	111	175
5.50	74	80	73	55	89	150
6.00	63	65	70	49	74	80
6.50	53e	50	59	51	62	80
7.00	47	27	51	47	53	35
7.50	41	15	44	43	46	35

colour–magnitude diagrams in the *Spitzer* bands, we used stellar evolution models with a detailed description of the AGB phase. The formation and growth of dust grains was described following the isotropic expansion of the stellar wind from the stellar surface. The magnitudes in the five IRAC and MIPS bands were calculated by convolution of the synthetic spectra with the instrumental transmission curves of the different filters. In the following part of this section, we give more details of the steps required.

## 2.1 Stellar evolution modelling

The stellar evolution models were calculated by means of the `ATON` code for stellar evolution. The interested reader may find a detailed description of the numerical and physical input of the code in Ventura et al. (1998); the most recent updates, concerning in particular the adopted cross-sections for the reactions included in the nuclear network, can be found in Ventura & D’Antona (2009). The evolutionary sequences were calculated from the pre-main-sequence phase until the almost complete loss of the star’s hydrogen envelope (the end of the AGB phase). To follow the different populations present in the LMC, we considered three different sets of models, with metallicity  $Z = 10^{-3}$ ,  $4 \times 10^{-3}$  and  $8 \times 10^{-3}$ . In the first case, we adopted an  $\alpha$ -enhancement  $[\alpha/\text{Fe}] = +0.4$ , whereas for the two more metal-rich models we used  $[\alpha/\text{Fe}] = +0.2$ . The initial abundances of elements other than  $\alpha$ -elements and carbon are scaled accordingly from the solar abundance (Grevesse & Sauval 1998) to the Fe abundance.

The physical properties of the three sets of models and the variation of their surface elemental abundance as they evolve on the AGB are extensively discussed in the previous articles published by our group (Ventura et al. 2013, 2014b). In Table 1, we report the evolutionary time-scales of the various stellar models considered, in terms of the duration of the core hydrogen-burning phase ( $\tau_{\text{ev}}$ ) and the whole AGB phase ( $\tau_{\text{AGB}}$ ). The latter time-scale was determined by considering the time elapsed from the phase following the exhaustion of central helium to the total loss of the external mantle.

We briefly recall the main physical and chemical input most relevant for the description of the AGB phase.

(i) The temperature gradient in regions unstable to convective motions was found by means of the full spectrum of turbulence (FST) model developed by Canuto & Mazzitelli (1991). As discussed extensively by Ventura & D’Antona (2005), use of the FST scheme leads to strong hot bottom burning (HBB) in models with initial mass above  $\sim 3 M_{\odot}$ ; the ignition of HBB favours severe destruction of the surface carbon (Ventura & D’Antona 2005), which prevents the star from reaching the C-star stage.

(ii) In convective regions, mixing of chemicals and nuclear burning are coupled self-consistently via a diffusive approach (Cloutmann & Eoll 1976). Overshoot from convective borders is simulated by an exponential decay of convective velocities from the neutrality layer, fixed via the Schwarzschild criterion (Freytag, Ludwig & Steffen 1996). During the core H- and He-burning phases, we assumed an e-folding distance for the exponential decay of velocities from the border of the core of  $0.02H_p$ , where  $H_p$  is the pressure scaleheight; this was obtained by comparison of the theoretical isochrones with the open cluster colour–magnitude diagram by Ventura et al. (1998). During the AGB phase, some overshoot is assumed from the borders of the convective shell that develops during the thermal pulse (TP) and from the base of the convective envelope; in this case, the e-folding distance is  $0.002H_p$ , following a calibration aimed at reproducing the luminosity function of carbon stars in the LMC, given in Ventura et al. (2014a).

(iii) Mass loss was described following the description by Blöcker (1995) in all AGB phases before the C-star phase begins. This treatment, based on hydrodynamic simulations by Bowen (1988), assumes a steep dependence of mass loss on luminosity ( $\dot{M} \sim L^{4.7}$ ). Consequently, stars experiencing HBB are expected to lose mass at large rates. For carbon stars, we used the formula giving the mass-loss rate as a function of luminosity and effective temperature for the LMC from the Berlin group (Wachter et al. 2002, 2008). This treatment is based on pulsating hydrodynamical models, in which mass loss is driven by radiation pressure on dust grains.

(iv) The molecular opacities in the stellar surface layers (temperatures below 10 000 K) were calculated by means of the `AESOPUS` (Marigo & Aringer 2009), which is necessary because of the increase in opacity of the external regions when the mixture becomes enriched in carbon; this is mainly due to the formation of CN molecules that occurs when the C/O ratio becomes larger than unity (Marigo 2002). The tables generated with the `AESOPUS` code are available for the range of temperatures  $3.2 \leq \log T \leq 4.5$ . The reference tables assume the same initial composition of the models as used in the present work. For each combination of metallicity and  $\alpha$ -enhancement, additional tables are generated, in which the reference mixture is altered by varying the abundances of C, N and O. This step is performed by introducing the independent variables  $f_C$ ,  $f_N$  and  $f_{CO}$ , corresponding to the enhancement (in comparison with the initial stellar chemistry) of carbon, nitrogen and C/O ratio, respectively. In each stellar layer, the opacity is found via interpolation on the basis of the values of temperature and density and of the mass fractions of the CNO elements. Ventura & Marigo (2009, 2010) showed that once the star enters the C-star phase the surface layers expand, which accelerates loss of the remaining hydrogen envelope, owing to the increase in the rate at which mass loss occurs.

## 2.2 Dust formation in the winds of AGBs

The winds of AGBs are rather cool, given the small effective temperatures ( $T_{\text{eff}}$  below  $\sim 4000$  K); in these cool winds, dust particles can form more easily in regions sufficiently close to the surface of the star (typically at distances in the range  $1-10R_*$ , where  $R_*$  is the stellar radius), where the densities are large enough to allow atoms and molecules to condense into dust grains. Towards the end of their evolution, the effective temperature of AGBs decreases considerably, as a consequence of the loss of their external envelope; this effect is stronger in carbon stars, owing to the gradual enrichment in carbon of their surface layers, which leads to a general cooling of the whole zone close to the surface (Marigo 2002). Therefore, in the final phases of their life AGBs suffer very large mass-loss rates, which also contribute to forming large quantities of dust, because more gas particles are available for condensation. In a self-consistent approach, mass loss should be calculated based on the dust formed and the interaction of dust particles with radiation pressure. However, in the simple schematization adopted here, mass loss is assumed *a priori* as a boundary condition. An interested reader may find an exhaustive discussion on this limitation in Ventura et al. (2014a).

In the present work, the growth of dust particles is calculated with a simple model for the stellar wind. The outflow is assumed to be spherically symmetric and to have an initial expanding velocity from the surface of the star of  $v = 10^5 \text{ cm s}^{-1}$ . The description is done via a set of equations describing the rate of growth of each individual dust species (starting from the innermost point where it forms). These relations are completed by mass and momentum conservation. Mass conservation allows us to determine the radial density of the gas (see e.g. equation 2 in Ventura et al. 2014a). The equation of momentum conservation considers the acceleration of the gas particles due to the effects of radiation pressure on the grains already formed; it allows a description of the increase in velocity of the wind after dust formation begins, until an asymptotic value is reached (typically from  $5-30 \text{ km s}^{-1}$ , as observed in AGB stars: Knapp & Morris 1985). The necessary input for the description of the wind is the evolutionary status of the central object: the effective temperature, luminosity, mass-loss rate and surface chemical

composition, particularly the C/O ratio. An interested reader may find all the relevant equations in Ventura et al. (2012a,b, 2014a) and Di Criscienzo et al. (2013), along with a discussion of the various uncertainties affecting the robustness of this approach, which is based on the pioneering explorations by the Heidelberg group (Gail & Sedlmayr 1985, 1999; Ferrarotti & Gail 2001, 2002, 2006; Zhukovska et al. 2008) and was also adopted in more recent investigations by Nanni et al. (2013a,b, 2014).

A common result from all these investigations is that, in the winds of oxygen-rich stars, formation of silicates occurs at a distance that, depending on the effective temperature, is in the range  $d \sim 5-10R_*$  from the stellar surface; small quantities of solid iron are also present. Dell’Agli et al. (2014b) find that the most stable dust species (alumina dust,  $\text{Al}_2\text{O}_3$ ) in oxygen-rich stars form at a typical distance of  $d \sim 1-3$  stellar radii from the stellar surface. The quantity of alumina dust formed is extremely sensitive to the amount of aluminium in the circumstellar envelope. Silicon is more abundant than aluminium at the surface of AGBs. Therefore, silicates, though less stable, form in larger quantities compared with alumina grains and represent the dominant compound produced by oxygen-rich stars; in addition, alumina is highly transparent to radiation and thus the wind is only barely accelerated by radiation pressure on  $\text{Al}_2\text{O}_3$  grains.

In carbon-rich environments we find a similar situation (Dell’Agli 2012), with a stable and extremely transparent dust species, silicon carbide (SiC), forming close to the surface of the star ( $d \sim 1-2R_*$ ), surrounded by a more external region ( $d \sim 5R_*$ ) where solid carbon grains form and grow (see fig. 4.2 in Dell’Agli 2012). The latter species form in much greater quantities than SiC, owing to the much greater availability of carbon atoms in comparison with silicon. Also, in this case some solid iron can form.

To calculate the extinction coefficients entering the momentum equation and the synthetic spectra, as described in next section, we used the following optical constants: for silicates, we used results from Ossenkopf, Henning & Mathis (1992); for corundum, we used Koike et al. (1995); for iron, we adopted the optical constants from Ordal et al. (1988); for SiC, we used results based on the compilation by Pegourie (1988); finally, results from Jaeger et al. (1994) were used for solid carbon.

Formation of silicates (oxygen-rich stars) and carbon (C-star) particles favours a strong acceleration of the wind, the velocity of which rapidly reaches an asymptotic behaviour. On the mathematical side, this allows us to limit the computations to a region sufficiently far from the surface of the star ( $d \sim 100R_*$ ), beyond which the velocity of the wind and the size of the dust species considered undergo only minor changes.

## 2.3 Synthetic spectra

The modelling of the AGB phase, discussed in Section 2.1, allows us to determine the variation with time of the main physical quantities of the central star, namely the luminosity, effective temperature, surface gravity and rate at which mass loss occurs. At the same time, we follow the variation of the surface elemental abundances for the species included in our network (from hydrogen to silicon). Because the nucleosynthesis in AGBs is limited to species lighter than silicon, we assume that the iron content remains unchanged during the whole evolution. We use all these ingredients, along with the results of dust formation models, to calculate synthetic spectra for some selected points along the evolutionary tracks; this step allows us to determine the magnitudes in the various bands, via convolution with the corresponding transmission curves.

The synthetic spectra were calculated in two steps, by means of the code *DUSTY* (Nenkova, Ivezić & Elitzur 1999).

(i) For carbon stars, we first considered the region from the surface up to the beginning of the solid carbon formation zone. In this preliminary step, the only dust species considered is SiC. As input radiation, we used the spectral energy distribution found by interpolation in surface gravity, effective temperature and C/O ratios among COMARCSatmospheres (Aringer et al. 2009) of the appropriate metallicity. An analogous procedure was followed for oxygen-rich stars, with the difference that the only species considered is alumina and the input spectrum is obtained by interpolating among NEXTGENatmospheres (Hauschildt et al. 1999) of the same metallicity; in this case the computations are extended until the formation of silicates begins.

(ii) The spectral energy distribution obtained in step (i), emerging from the SiC (alumina) dust layer for C stars (oxygen-rich stars), is used as input for the second layer, where we consider the reprocessing of radiation by SiC and solid carbon for C stars (alumina and silicates for oxygen-rich stars).

The inputs necessary to steps (i) and (ii) are not assumed *a priori*; they are found via the description of dust formation in the wind, discussed in Section 2.2, which allows the determination of the dust grain size and composition, the temperature of the region where the various dust species form and the radial distribution of the gas density. Concerning the latter point, although we know the radial variation of the dimension of the dust particles, we use a single grain size for each species, corresponding to the asymptotic value reached. This choice is motivated by the fact that the asymptotic value is reached rapidly once the dust begins to form, thus leading to a grain size distribution strongly peaked towards such an asymptotic value. To determine the optical depth,  $\tau_{10}$ , we integrate along the radial direction the product of the number density of dust particles and the extinction cross-section, based on knowledge of the optical constants and grain size.

To compare the fluxes observed with those found via our spectral analysis, we adopted a distance to the LMC of 50 kpc (Feast 1999).

### 3 EVOLUTIONARY PROPERTIES AND SPITZER COLOURS OF AGB STARS

The spectra of AGB stars change during their evolution, owing to variation in effective temperatures, luminosities and the composition and mass of dust grains in the circumstellar envelopes. The C/O ratio is the relevant quantity to assess whether carbon dust or silicates form.

The surface content of carbon and oxygen changes during the AGB phase under the effects of the two physical processes that are able to alter the elemental abundance of the circumstellar envelope: HBB and third dredge-up (TDU; Herwig 2005). In the first case, we have the activation of advanced proton-capture nucleosynthesis at the bottom of the convective envelope (Renzini & Voli 1981; Blöcker & Schönberner 1991). The elemental abundances change via an enhanced CN cycle, with an increase in nitrogen content at the expense of carbon and (for temperatures above  $\sim 50$ – $60$  MK) oxygen. The third dredge-up, occurring immediately after each TP, consists of the inwards penetration of the convective envelope down to regions of the star previously touched by  $3\alpha$  nucleosynthesis: the main effect of TDU is the increase in surface carbon.

We analyse separately the main evolutionary features of AGB models dominated by each mechanism.

#### 3.1 The effects of hot bottom burning

In stars with initial mass above  $\sim 3 M_{\odot}$  the occurrence of HBB keeps the C/O ratio below unity, because carbon is destroyed via proton capture at the bottom of the convective envelope. This threshold mass partly depends on the metallicity, being  $3 M_{\odot}$  for  $Z = 8 \times 10^{-3}$  and  $2.5 M_{\odot}$  for  $Z = 10^{-3}$  (Ventura et al. 2013). Stars of mass above this limit never become carbon stars, thus the only dust particles formed in their winds are alumina and silicates.<sup>1</sup> The surface abundances of the key particles for these dust species, i.e. aluminium and silicon, remain practically constant during the AGB phase,<sup>2</sup> thus dust formation is mainly driven by the strength of HBB. Strong HBB favours a considerable increase in the luminosity and mass-loss rate, which, in turn, increases the density of gas particles available for dust formation in the wind (Ventura et al. 2012a).

The evolution of the luminosity and mass-loss rate of models with initial mass  $M > 3 M_{\odot}$  is shown in Fig. 1. For reasons of clarity, we only show the 3.5-, 4.5-, 5.5- and 6.5- $M_{\odot}$  cases. We focus on models with metallicity  $Z = 8 \times 10^{-3}$ , because (i) stars within this range of mass have ages lower than  $\sim 2 \times 10^8$  yr and were born in an epoch when most of the stars formed in the LMC have metallicity  $Z \geq 4 \times 10^{-3}$  (see the discussion on the SFH used in the present work for the LMC in Section 5.3) and (ii) in models of lower metallicity, owing to scarcity of silicon, dust is produced at lower rates in comparison with more metal-rich stars: the highest rate found in the  $Z = 10^{-3}$  case is  $\dot{M}_d \sim 3 \times 10^{-8} M_{\odot} \text{ yr}^{-1}$ , whereas in the  $Z = 8 \times 10^{-3}$  models typical values are above  $\dot{M}_d \sim 2 \times 10^{-7} M_{\odot} \text{ yr}^{-1}$  (Ventura et al. 2012b).

We see in Fig. 1 (left panel) that models of higher mass evolve at larger luminosities; this is because the higher the initial mass of the star, the heavier the core mass becomes and hence the higher the luminosity a star can reach (Paczynski 1970). Also, they experience stronger HBB. The luminosity reaches a maximum during AGB evolution, then decreases, because of the gradual loss of the external mantle. The higher the initial mass, the more quickly the star reaches the maximum luminosity.

Within the scheme we apply to describe dust formation, where the mass-loss rate is adopted as a boundary condition, we find that the amount of dust produced increases with initial stellar mass, because more massive models suffer higher mass-loss rates (see the right panel of Fig. 1). This is a straight consequence of the mass conservation law, on the basis of which higher mass-loss rates favour higher densities, thus more gas molecules are available for condensation. Therefore, having more dust formed at the inner region, stars with higher initial masses tend to emit higher fluxes at mid-infrared wavelengths. These oxygen-rich stars emit the largest mid-infrared flux during the phase of maximum luminosity, when mass is lost at the highest rates. However, as shown in Dell’Agli

<sup>1</sup> This conclusion holds as far as convection is modelled within the FST framework. When the traditional mixing-length scheme is adopted, the temperatures at the bottom of the convective envelope are smaller and the strength of HBB is consequently reduced, thus the range of masses potentially able to reach the C-star stage is larger (Ventura & D’Antona 2009; Doherty et al. 2014).

<sup>2</sup> This holds strictly for stars with  $Z \geq 8 \times 10^{-3}$ , where the temperatures at the bottom of the surface convection zone do not allow any Mg–Al nucleosynthesis (Ventura et al. 2013). For metallicities  $Z \leq 10^{-3}$ , massive AGBs are expected to increase the surface aluminium by a factor of 10 and to increase the silicon content by  $\sim 10$ – $20$  per cent (Ventura, Carini & D’Antona 2011). However, at these low metallicities only a modest production of dust is expected, owing to the small abundances of the key elements required to form dust.

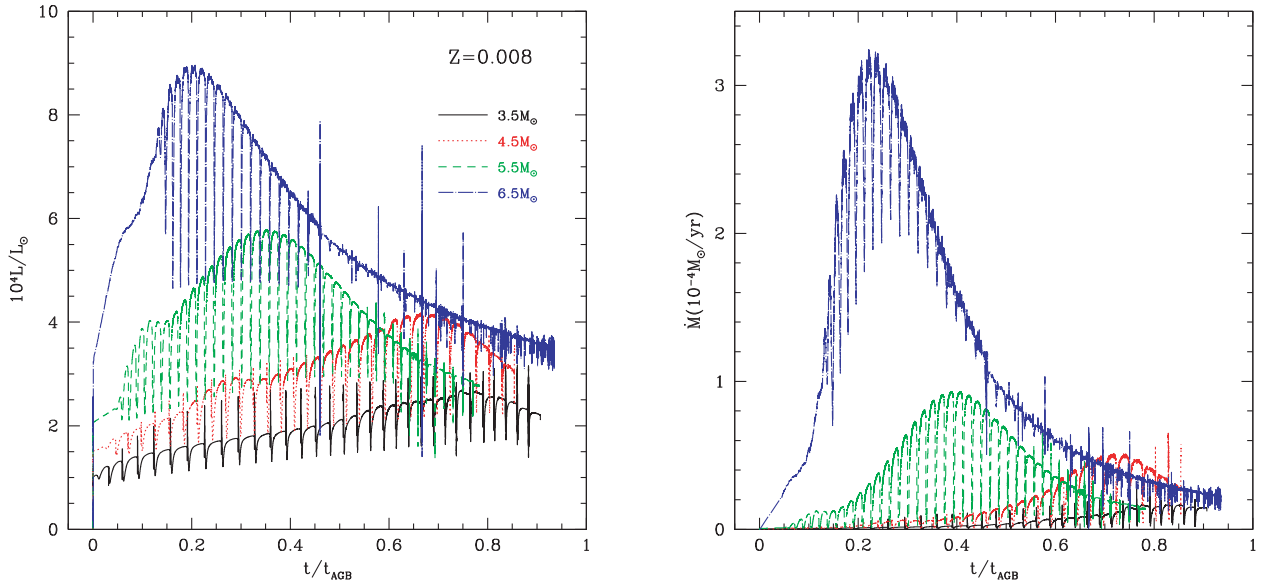


**Figure 1.** The variation of luminosity (left) and mass-loss rate (right) of models of different initial mass during the AGB phase. Times are normalized to the total duration of the AGB phase for each mass, indicated in Table 1. The various tracks refer to models of metallicity  $Z = 8 \times 10^{-3}$  and initial mass  $3.5 M_{\odot}$  (black, solid track)  $4.5 M_{\odot}$  (red, dotted),  $5.5 M_{\odot}$  (green, dashed) and  $6.5 M_{\odot}$  (blue, dot-dashed). [A colour version of this figure is available in the online version.]

et al. (2014a, see their fig. 1), the optical depth of these models will not be decreased significantly during the following AGB phases, because the decrease in mass-loss rate is partly counterbalanced by the smaller effective temperatures towards the final AGB stages, which favour the formation and growth of dust grains.

### 3.2 The AGB evolution towards the C-star regime

In stars with  $M < 3 M_{\odot}$ , repeated episodes of third dredge-up favour a gradual increase in surface carbon, eventually leading to the formation of carbon stars. The possibility of reaching the C-star stage not only depends on whether HBB is active but also requires that, at the photosphere, the abundance of carbon exceeds that of oxygen before the hydrogen envelope is completely lost. The range of masses that become carbon stars is  $1.25 M_{\odot} \leq M < 3 M_{\odot}$ .<sup>3</sup>

Stars of  $M \leq 1 M_{\odot}$  never become carbon stars. They evolve as oxygen-rich stars throughout their AGB phase. Their surface chemistry is changed only by the first dredge-up, which occurs while ascending the red giant branch.

In the two panels of Fig. 2 we show the difference between the number densities of carbon and oxygen nuclei in AGB models with metallicity  $Z = 8 \times 10^{-3}$  (left) and  $10^{-3}$  (right). The difference is normalized to the density of hydrogen atoms, i.e.  $\epsilon_{C,O} = n_{C,O}/n_H$ . This quantity indicates the efficiency with which the surface envelope is enriched in carbon and is strongly related to the amount of solid carbon formed. Unlike their more massive counterparts, here we show both the highest and the lowest metallicities of LMC stars. Indeed, these low-mass stars evolve slowly, with a time-scale of 0.3–15 Gyr. Within this time-scale, the LMC has formed stars with a range of metallicities (see Table 1 and Fig. 4 later), which we represent with three metallicity grids from  $Z = 10^{-3}$  to  $8 \times 10^{-3}$ . Note that

<sup>3</sup> Indeed, in the  $Z = 10^{-3}$  case the  $3 M_{\odot}$  model ignites HBB, thus restricting the range of masses becoming carbon stars to  $M \leq 2.5 M_{\odot}$ .

Harris & Zaritsky (2009) also identified the  $Z = 2.5 \times 10^{-3}$  component, but we have binned this component together with the  $Z = 10^{-3}$  one. All the models with initial mass  $1.25 M_{\odot} < M < 3 M_{\odot}$  evolve initially as oxygen-rich stars, with  $C/O < 1$  (i.e.  $\epsilon_C - \epsilon_O < 0$ ). In the last fraction of the AGB evolution (ranging from  $\sim 30$  per cent to 70 per cent, depending on the values of  $M$  and  $Z$ ), they evolve as carbon stars. Due to the smaller initial oxygen abundance,  $\epsilon_C - \epsilon_O$  is, on average, larger for the  $Z = 10^{-3}$  population than for the high-metallicity counterpart. This causes the star to reach the carbon-rich phase earlier in its evolution. Models of higher mass ( $M \geq 2 M_{\odot}$ ) are more enriched in carbon, because they experience more TDU events; this trend with mass is reversed close to the limit for HBB ignition, because the models experience TDU episodes of smaller efficiency (Ventura et al. 2014a).

The increase in surface carbon has important feedback on the AGB evolution: the consequent increase in the molecular opacities favours an expansion of the surface layers with a decrease in surface temperature and an increase in the rate at which mass loss occurs (Ventura & Marigo 2009, 2010). This effect can be seen clearly in Fig. 3, showing the mass-loss rate experienced by stars of metallicity  $Z = 8 \times 10^{-3}$ , with initial mass  $1.25 \leq M \leq 3 M_{\odot}$ . We note the fast increase in  $\dot{M}$  in the very latest evolutionary phases, associated with the increase in surface carbon (see left panel of Fig. 2). The cooling of the external regions and the increase in the mass-loss rate concur in forming larger quantities of carbon grains, leading to a progressive obscuration of the radiation from the star. At odds with the stars experiencing HBB, here the colours become redder and redder as the stars lose the external mantle.

### 3.3 The infrared colours of AGBs: predictions from modelling

Fig. 5 shows the variation of the  $[3.6] - [4.5]$ ,  $[5.8] - [8.0]$  and  $[8.0] - [24]$  colours of AGB models with  $Z = 8 \times 10^{-3}$ . We consider stellar models with initial mass of  $1 M_{\odot}$  (representing low-mass stars never reaching the C-star stage),  $2 M_{\odot}$ ,  $3 M_{\odot}$

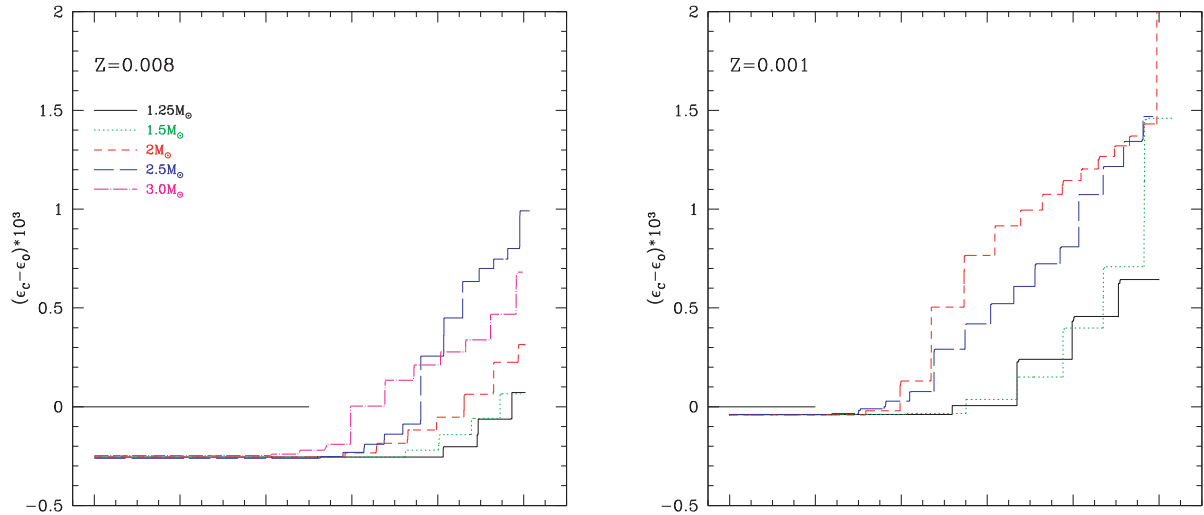


**Figure 2.** The evolution of the relative excess of carbon with respect to oxygen (see text for definition) during the AGB phase of stars with masses in the range  $1.25\text{--}3M_{\odot}$  and metallicity  $Z = 8 \times 10^{-3}$  (left panel) and  $10^{-3}$  (right). Times are normalized to the total duration of the AGB. Thin, horizontal lines indicate the  $C = O$  condition; tracks above these lines correspond to C stars. The values on the vertical axis when the abscissa is unity indicate the carbon excess reached at the very end of AGB evolution, when the envelope is lost.

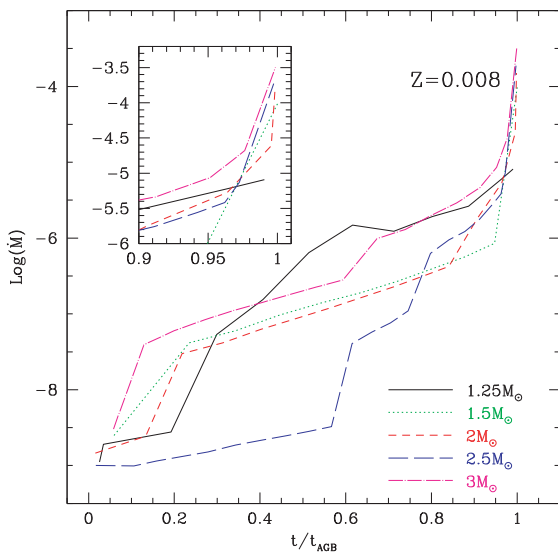


**Figure 3.** The variation of mass-loss rate experienced by stars reaching the C-star stage during AGB evolution. The models, of metallicity  $Z = 8 \times 10^{-3}$ , are the same as shown in the left panel of Fig. 2. In the inset we show a zoom of the mass-loss rate at the end of the AGB phase.

(C stars),  $4.5M_{\odot}$ ,  $5.5M_{\odot}$  and  $6.5M_{\odot}$  (these models experience HBB).

In the left panel of Fig. 5, we note that, for the  $2M_{\odot}$  and  $3M_{\odot}$  models,  $[3.6] - [4.5]$  starts to increase once the C-star stage is reached, as a consequence of the progressive enrichment in carbon of the external layers. This phase encompasses about  $\sim 30$  per cent of the total AGB evolution. In the very latest evolutionary phases, the outermost regions of the star become cooler and cooler, with effective temperatures of the order of  $\sim 2000$  K. During these phases, the star loses mass at large rates (see Fig. 3) and great quantities of carbon dust are present in the circumstellar envelope; this, in turn, determines a strong obscuration of the stellar radiation. This is the reason for the rapid increase in  $[3.6] - [4.5]$ , which reaches

a maximum of  $\sim 3$  for the  $2.5M_{\odot}$  (not shown) and  $3M_{\odot}$  models. This sequence of events is shown for a  $2.5M_{\odot}$  model in the left panel of Fig. 6: we see that the SED is progressively shifted to longer wavelengths as the surface carbon increases. Note that, in the final stages of the AGB phase (here represented by the green line), the emission SiC feature at  $11.3\ \mu\text{m}$  turns into an absorption feature.

In the  $2M_{\odot}$  case, the reddest value reached is smaller ( $[3.6] - [4.5] \sim 1.6$ ), owing to the lower amount of carbon available in the envelope (see left panel of Fig. 2). The duration of these phases characterized by thermal emission of dust is within  $\sim 5$  per cent of the total AGB life.

Models with mass above  $3M_{\odot}$  never become carbon stars and follow a different behaviour. The thermal emission from dust is lower, owing to the smaller extinction coefficients of silicates in comparison with carbon grains:  $[3.6] - [4.5] < 0.5$  in all cases. The discussion in Section 3.1 outlined that in these stars the maximum luminosity, when the star experiences the highest mass-loss rates, is reached at an intermediate phase during the AGB evolution. This is also the phase when the largest quantities of dust are formed in the circumstellar envelope. Therefore, the trend of  $[3.6] - [4.5]$  is not a monotonic increase in time: the reddest values are achieved at this phase of maximum dust production, when HBB is experienced. The highest values in the left panel of Fig. 5 correspond to the maximum luminosities in Fig. 1.

In the  $1M_{\odot}$  case, the  $[3.6] - [4.5]$  colour shows a gradual increase in time, owing to the progressively higher rate with which silicates form, which, in turn, shifts the SED to longer wavelengths. The thermal emission from dust is small in this case, with  $[3.6] - [4.5] < 0.2$  for the entire evolution.

The  $[5.8] - [8.0]$  colour for the C-star models follows a behaviour similar to  $[3.6] - [4.5]$ . In this case the largest values, reached in the latest phases, are  $[5.8] - [8.0] \sim 1.8$  for both  $2.5M_{\odot}$  and  $3M_{\odot}$  models. The difference between the reddest colours reached by C and oxygen-rich stars is smaller than for  $[3.6] - [4.5]$ , because the formation of the silicate feature in O-rich objects at  $9.7\ \mu\text{m}$  favours an increase in  $[8.0]$  flux, making  $[5.8] - [8.0]$  redder. During the phase of strongest HBB of O-rich models,

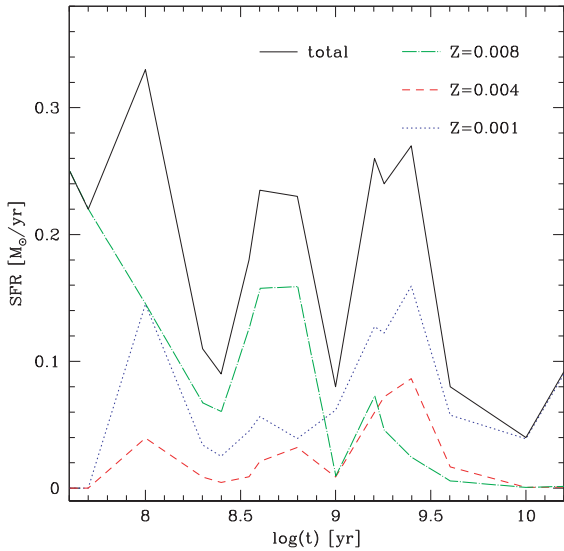


**Figure 4.** The time variation of the star formation rate in the LMC according to Harris & Zaritsky (2009). The different lines give the total star formation rate (black, solid track) and the fractional contribution of metallicities  $Z = 8 \times 10^{-3}$  (green, dot-dashed),  $Z = 4 \times 10^{-3}$  (red, dashed) and  $Z = 10^{-3}$  (blue, dotted), as given in Harris & Zaritsky (2009). The latter component here represents the cumulative contribution of the two  $Z = 10^{-3}$  and  $Z = 2.5 \times 10^{-3}$  tracks of the original Harris & Zaritsky (2009) SFH. [A colour version of this figure is available in the online version.]

$[5.8] - [8.0] \sim 1$ . The  $1-M_{\odot}$  model not experiencing HBB only reaches  $[5.8] - [8.0] \sim 0.6$ .

The  $[8.0] - [24]$  colours also become redder and redder as the amount of dust formed in the envelope gets larger and the total flux from dust thermal radiation increases. C-star models exhibit the same behaviour as in the other colours. The amount of excess carbon with respect to oxygen in the atmosphere reaches its highest value at the end of the AGB phase, resulting in a steep rise in the amount of carbon dust formed. The  $[8.0] - [24]$  colour becomes red, reaching a final value of  $\sim 3$ . The trend followed by oxygen-rich stars is qualitatively different. In models experiencing HBB, as in other colours, the reddest values are reached in conjunction with the phase of maximum efficiency of HBB; however, in lower mass models

not experiencing HBB,  $[8.0] - [24]$  reaches a maximum value slightly below  $\sim 2$  and decreases subsequently, when formation of the silicate feature increases the  $[8.0] \mu\text{m}$  flux.

### 3.4 Dusty AGB models: theoretical tracks

Fig. 7 shows the evolutionary tracks of models of different mass in the colour–colour ( $[3.6] - [4.5]$ ,  $[5.8] - [8.0]$ ) (left panels, hereinafter CCD1) and ( $[3.6] - [8.0]$ ,  $[8.0] - [24]$ ) (right, hereinafter CCD2) planes. Fig. 8 shows the same tracks in the colour–magnitude ( $[8.0] - [24]$ ,  $[24]$ ) (left) and ( $[3.6] - [8.0]$ ,  $[8.0]$ ) (right) diagrams (hereinafter CMD24 and CMD80). The top panels refer to  $Z = 8 \times 10^{-3}$  models, while the tracks of  $Z = 10^{-3}$  stars are shown in the bottom panels.

The sequences of carbon stars and oxygen-rich models bifurcate in the CCD1 and CCD2 planes, the oxygen-rich stars tracing a more vertical sequence. This can be seen in the top panels of Fig. 7, by comparing the tracks of the 4-, 5.5- and  $6.5-M_{\odot}$  models with those of their  $M \leq 3 M_{\odot}$  counterparts. The bifurcation between C-rich and oxygen-rich models is also evident in CMD80, shown in the right panels of Fig. 8. This behaviour can be understood on the basis of the discussion in Section 3.3: in O-rich stars the formation of the silicate feature at  $9.7 \mu\text{m}$  leads to a decrease in the  $[8.0]$  magnitude. This provides a straight explanation for the high slope of the corresponding tracks in the CMD80 plane and favours redder  $[5.8] - [8.0]$  (see Fig. 5) and  $[3.6] - [8.0]$  colours.

Metallicity has important effects on the excursion of the evolutionary tracks in these planes. First, concerning oxygen-rich stars, models of higher metallicity reach redder colours in the CCD1 and CCD2 planes. The comparison between the tracks of the  $Z = 10^{-3}$  and  $Z = 8 \times 10^{-3}$  models in CCD1 shows that, while massive AGBs of the latter population evolve up to colours  $[5.8] - [8.0] \sim 1$ , their lower- $Z$  counterparts, with the exception of Super Asymptotic Giant Branch (SAGB) models with initial mass above  $\sim 6 M_{\odot}$ , barely reach  $[5.8] - [8.0] \sim 0.5$ . In CCD2, higher- $Z$ , massive AGBs evolve to  $[8.0] - [24] \sim 2$ , while their  $Z = 10^{-3}$  counterparts reach  $[8.0] - [24] \sim 1.5$ . These differences originate in the larger quantities of dust formed in the envelopes of higher metallicity stars, as a consequence of the larger amount of silicon available. The analysis of the colour–magnitude diagrams, shown in Fig. 8, confirms that oxygen-rich stars with higher metallicity evolve to redder infrared

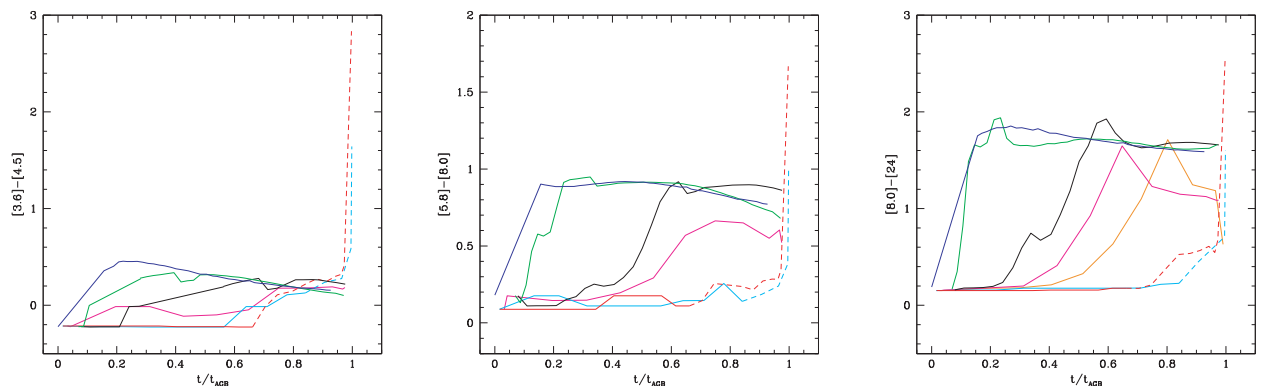


**Figure 5.** Evolution of the colours  $[3.6] - [4.5]$  (left panel),  $[5.8] - [8.0]$  (middle),  $[8.0] - [24]$  (right) during the AGB phase of models of metallicity  $Z = 8 \times 10^{-3}$  and initial masses  $1 M_{\odot}$ ,  $2 M_{\odot}$ ,  $3 M_{\odot}$ ,  $4.5 M_{\odot}$ ,  $5.5 M_{\odot}$  and  $6.5 M_{\odot}$ . In the right panel we also show the  $1.25 M_{\odot}$  model. Dashed tracks indicate carbon stars, while solid lines indicate oxygen-rich stars. Times are normalized to the total duration of the AGB phase [A colour version of this figure is available in the online version, where the various masses are indicated as follows:  $1 M_{\odot}$  (magenta),  $1.25 M_{\odot}$  (orange),  $2 M_{\odot}$  (cyan),  $3 M_{\odot}$  (red),  $4.5 M_{\odot}$  (black),  $5.5 M_{\odot}$  (green),  $6.5 M_{\odot}$  (blue)].

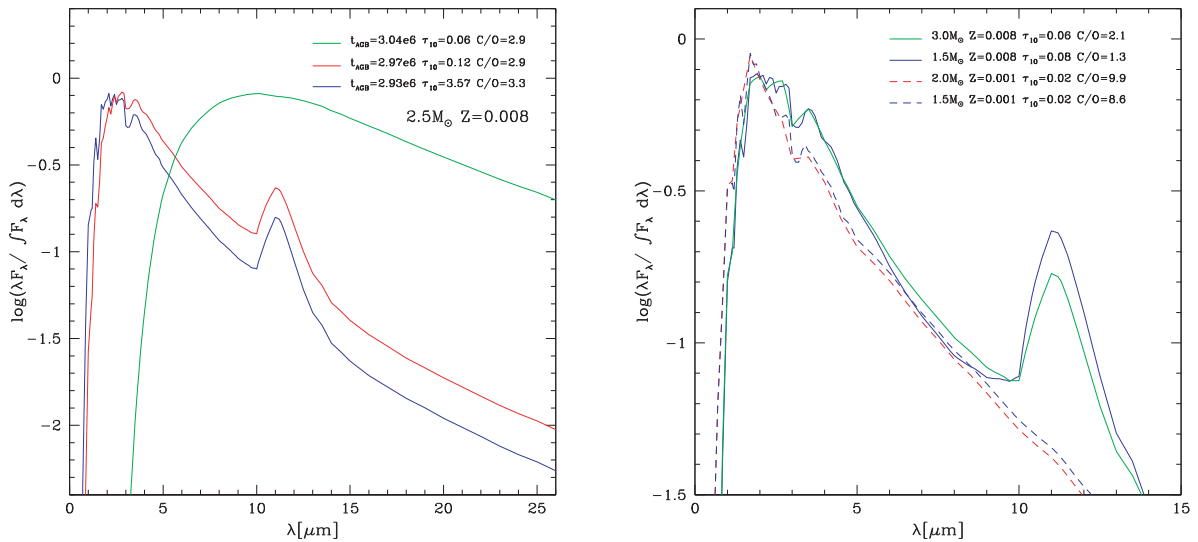


**Figure 6.** Left: The change in the spectral energy distribution of a model with initial mass  $2.5 M_{\odot}$  during the AGB phase. Right: The SED of models of various mass and metallicity, taken at  $[3.6] - [4.5] = 0.3$ .

(IR) colours. Not only do the tracks of the  $Z = 8 \times 10^{-3}$  models reach higher  $[3.6] - [8.0]$  and  $[5.8] - [8.0]$  colours, but also the 8.0- and 24- $\mu\text{m}$  fluxes are larger than their  $Z = 10^{-3}$  counterparts, as a consequence of the reprocessing of stellar radiation by silicate grains in the circumstellar envelope.

The metallicity of the stars also influences the distribution of carbon stars in the various planes. As shown in Fig. 7, C-rich objects of different metallicity define similar trends, with the difference that the  $Z = 8 \times 10^{-3}$  models evolve to redder colours. While for these stars we find that the tracks reach  $[3.6] - [4.5] \sim 3$ ,  $[3.6] - [8.0] \sim 7$ ,  $[8.0] - [24] \sim 2.5$ ,  $[5.8] - [8.0] \sim 7$ , in the  $Z = 10^{-3}$  case, despite the carbon excess reached being larger (see Fig. 2), we have  $[3.6] - [4.5] < 1$ ,  $[3.6] - [8.0] < 2.5$ ,  $[8.0] - [24] < 1$ ,  $[5.8] - [8.0] < 2$ . This is because lower- $Z$  stars evolve at higher effective temperatures, pushing the dust-forming layer far away from the stellar surface into a region of smaller density, where dust formation occurs with a lower efficiency. These arguments outline the delicate interplay between the surface carbon abundance and the temperature of the external regions in determining the amount of carbon dust formed.

The evolution of  $Z = 8 \times 10^{-3}$  models of initial mass  $M \sim 1.25, 1.5 M_{\odot}$  deserves particular attention, as it will also be important in the interpretation of the observations. As shown in the left panel of Fig. 2, these stars evolve as oxygen-rich objects for most ( $\sim 70$ – $80$  per cent) of their AGB life and eventually become carbon stars. They do not reach extremely red colours, because their envelope is lost before great amounts of carbon are accumulated at the surface. Their tracks in the various planes present turning points, associated with the transition from M to C stars. This behaviour is particularly evident in the CMD24 plane (see top left panel of Fig. 8), where the track corresponding to the  $M \sim 1.25 M_{\odot}$  model (indicated with a black line) first moves to the red, then turns into the blue. The right panel of Fig. 9 shows the excursion of the track in more detail, whereas in the left panel we show the SED of the same model at different evolutionary phases. In the first part of the AGB evolution, the optical depth increases, owing to the larger and larger quantities of silicates formed in the circumstellar envelope. Consequently, the silicate feature at  $9.7 \mu\text{m}$  becomes more prominent during the evolution (see the various SEDs shown in the left panel of Fig. 9).

After becoming a C star, the optical depth decreases and the star evolves to the blue. This peculiar behaviour of low-mass AGBs is restricted to  $Z = 8 \times 10^{-3}$  models, because lower- $Z$  stars produce smaller quantities of silicates, thus their tracks are bluer (see the bottom left panel of Fig. 8).

The track of the  $1.5 M_{\odot} Z = 8 \times 10^{-3}$  model in CCD1 moves to the red as the surface carbon increases (see the blue line in Fig. 7). However, compared with the lower- $Z$  model with the same mass or models with the same metallicity but higher masses, the track occupies the lower side of CCD1: for a given  $[3.6] - [4.5]$ , the  $[5.8] - [8.0]$  is bluer. To understand this trend, we show in the right panel of Fig. 6 the SEDs of models of various mass and metallicity, at the evolutionary stage when  $[3.6] - [4.5] \sim 0.3$ . A clear difference between models of different metallicity is the SiC emission feature, almost absent in the  $Z = 10^{-3}$  models owing to the scarcity of silicon in the envelope. We also note that the optical depth of the  $1.5 M_{\odot}$  model ( $\tau_{10} = 0.08$ ) is slightly larger than that of the  $3 M_{\odot}$  star ( $\tau_{10} = 0.06$ ), despite the surface carbon being larger in the latter case. The higher carbon content in the  $3 M_{\odot}$  case favours larger quantities of dust particles in the regions of the envelope at temperatures  $\sim 1100$  K, the threshold value to allow condensation of gas molecules into solid carbon grains. However, this effect is more than counterbalanced by the higher acceleration experienced by the wind: compared with the  $1.5 M_{\odot}$  model, the profile of density is steeper; thus, a smaller contribution to the overall value of  $\tau_{10}$  is given by the outermost layers of the  $3 M_{\odot}$  model, in comparison with its smaller mass counterpart.

In the comparison between the dust composition of the circumstellar envelopes of the two models, we have a higher quantity of SiC in the  $1.5 M_{\odot}$  case; conversely, owing to the larger amount of carbon available at the surface, the  $3 M_{\odot}$  envelope is dominated by carbon dust. The SED of the  $1.5 M_{\odot}$  model (blue line in the right panel of Fig. 6), compared with the corresponding SED of the  $3 M_{\odot}$  star (green line), reflects more closely the shape of the SiC feature: the relative flux is higher at  $\sim 11 \mu\text{m}$  and declines more steeply at shorter wavelengths in the  $5$ – $8 \mu\text{m}$  region of the spectrum. While the  $[3.6] - [4.5]$  colour is not affected by these differences, the  $[5.8] - [8.0]$  results are bluer in these models, which motivates their different position in CCD1.

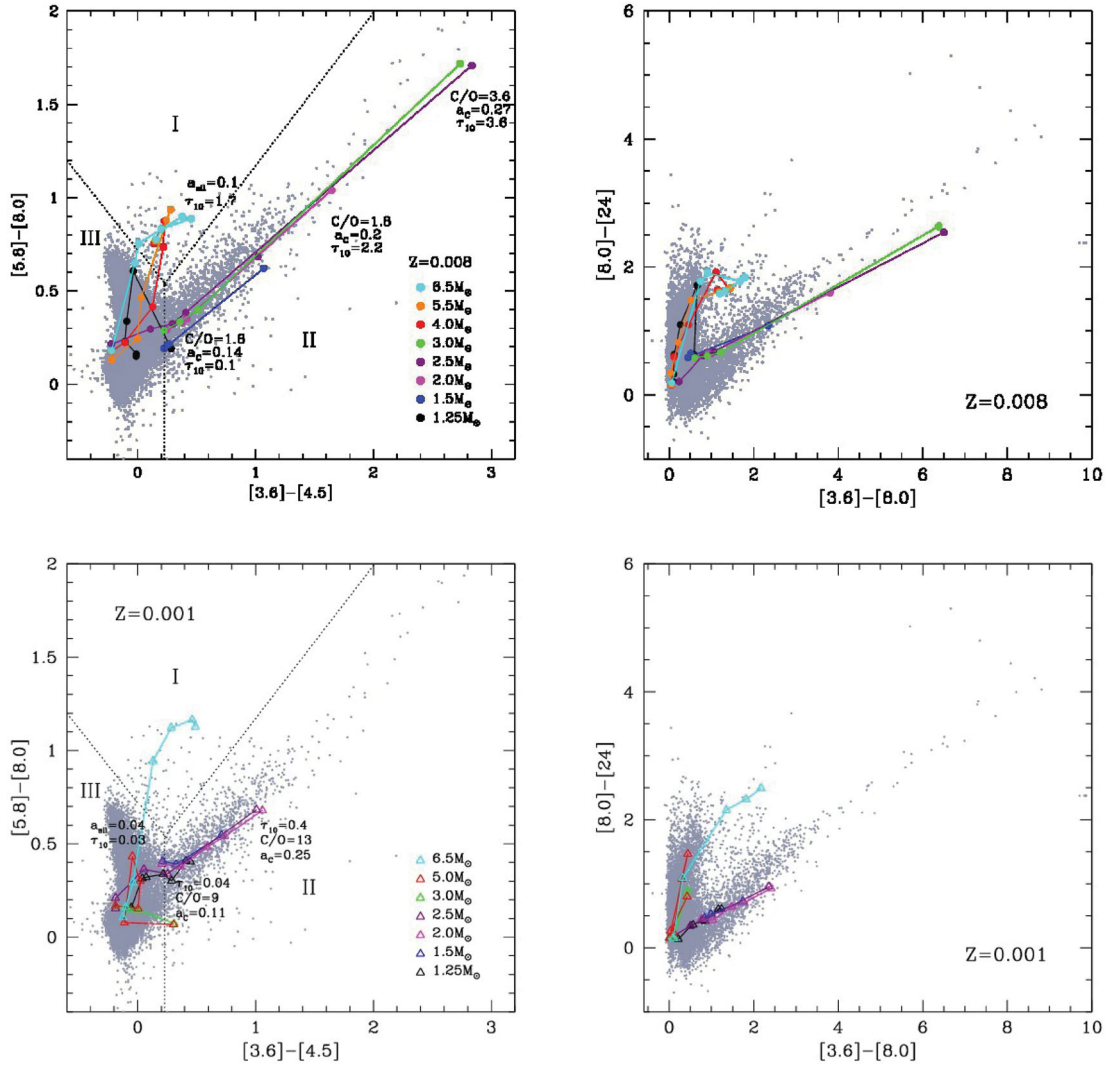


**Figure 7.** Evolutionary tracks of AGB models of metallicity  $Z = 8 \times 10^{-3}$  (top panels) and  $Z = 10^{-3}$  (bottom) in the colour–colour ( $[3.6] - [4.5]$ ,  $[5.8] - [8.0]$ ) (left) and ( $[3.6] - [8.0]$ ,  $[8.0] - [24]$ ) planes (right). The values of the optical depth  $\tau_{10}$ , C/O ratio and size (in  $\mu\text{m}$ ) of carbon grains (indicated with  $a_c$ ) and silicates particles ( $a_{\text{sil}}$ ) along some tracks are indicated. The diagrams in the left panels are divided into regions I, II and III, used to classify AGB stars (see the text in Section 4 for details).

#### 4 WHICH CLASSIFICATION FOR AGB STARS?

The results discussed in the previous section showed that AGB stars populate different regions in the colour–colour and colour–magnitude planes, depending on their mass, metallicity and optical depth. The evolutionary tracks are the outcome of complex computations of the AGB evolution and the dust formation process and are extremely sensitive to a number of physical inputs, such as convection, mass loss, treatment of convective borders and the entire description of the dust formation process. Assessing the reliability of these models demands comparison with observations, now possible thanks to several surveys of the LMC population of AGB stars described in the next section. This approach will hopefully help to reduce the uncertainties affecting the aforementioned physical mechanisms. To undertake this analysis, we need to identify groups of stars with specific properties that populate selected regions in the colour–colour and colour–magnitude planes obtained with the *Spitzer* bands.

We use the tracks presented and discussed in the previous section to propose a classification of AGB stars in the LMC into four

groups, each characterized by specific evolutionary properties and occupying well-defined regions in the CCD1, CCD2, CMD80 and CMD24 planes.

This classification is based on the following results, shown in Figs 7 and 8.

(i) The region on the upper side of CCD1, zone I in the left panels of Fig. 7, is populated exclusively by massive AGBs experiencing HBB, surrounded by silicates, with  $\tau_{10} > 0.1$ ; we will refer to these models as hot bottom burning stars (HBBS).

(ii) Zone II in CCD1 is populated by carbon stars with SiC particles and carbon dust in their envelopes and optical depth  $\tau_{10} > 0.02$ . We will refer to these models as obscured carbon stars (OCS).

(iii) The only tracks evolving in zone F in the CMD24 plane are those corresponding to low-mass stars,  $M \sim 1.25 M_{\odot}$ , in the phases preceding the C-star phase. We will call these models F stars (FS) in the following sections.

(iv) Region III in CCD1 is crossed by tracks of various mass and metallicity values, both oxygen- and carbon-rich. These models are not found to be significantly obscured. We will refer to them as

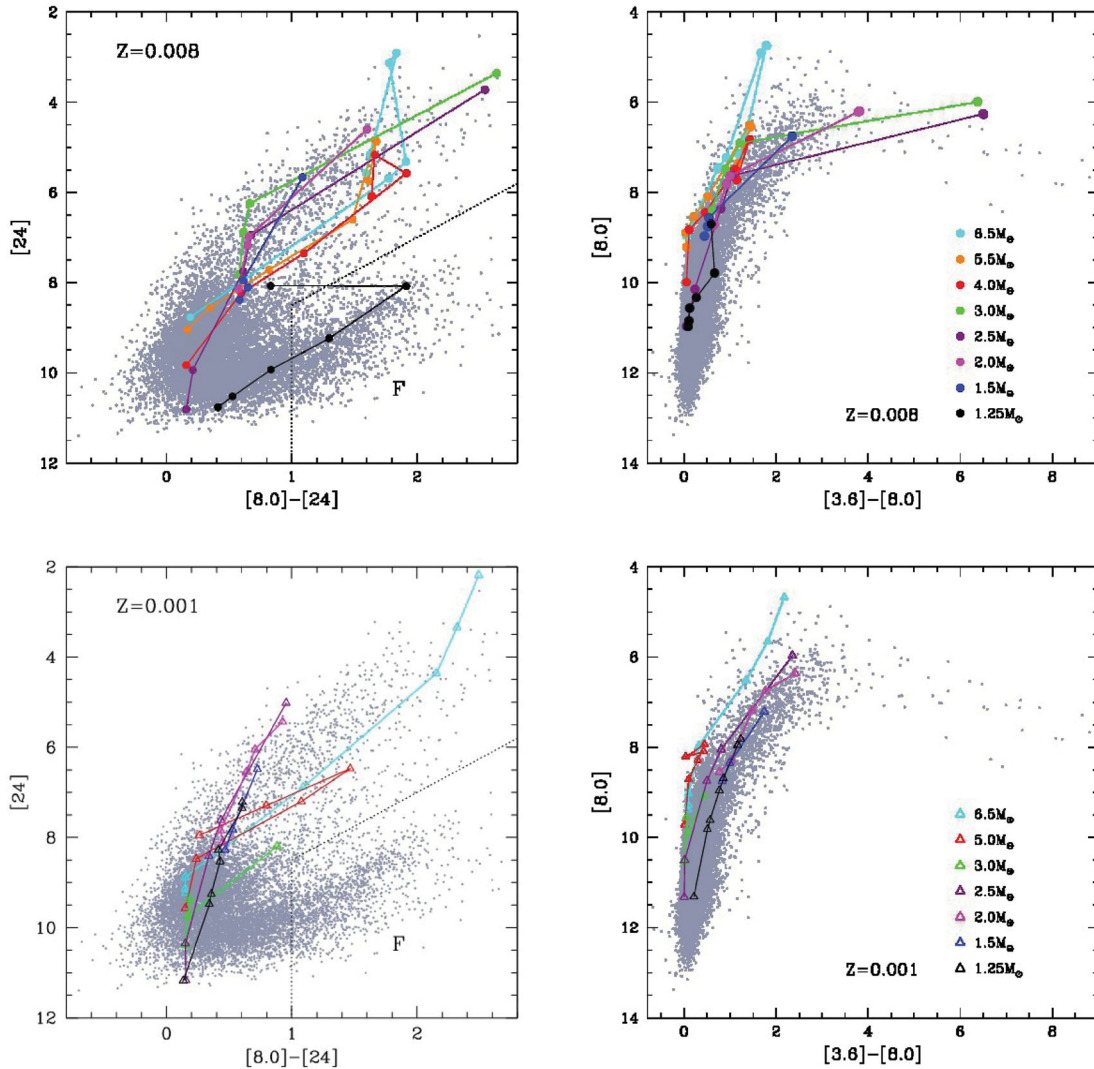


**Figure 8.** Evolutionary tracks of AGB models of metallicity  $Z = 8 \times 10^{-3}$  (top panels) and  $Z = 10^{-3}$  (bottom) in the colour–magnitude ( $[8.0] - [24]$ ,  $[24]$ ) (left) and ( $[3.6] - [8.0]$ ,  $[8.0]$ ) diagrams (right). In the left panels we show the region F, used for the classification of AGBs introduced in Section 4 (see text for details). The colour coding of the various tracks is the same as in Fig. 7.

C- and oxygen-rich stars (CMS) and they encompass all models not belonging to any of the three previous groups.

Both the observed sources and the models produced by the synthetic modelling will be classified according to the criteria given above, following their position in the CCD1 and CMD24 planes.

In the following section, we will describe the observational sample to be used for our analysis.

## 5 AGB STARS IN THE LMC: OBSERVATIONS AND THEORETICAL PREDICTIONS

### 5.1 Historical identification and classification of AGBs in the LMC

The first works aimed at the identification of the AGB population in the LMC were presented by Blanco, Blanco & McCarthy (1978), Richer & Westerlund (1983) and Frogel, Mould & Blanco (1990). More recently, Cioni et al. (2000a) attempted a classification of the AGB sample of the LMC based on  $IJKs$  data of over one

million point sources in the direction of the LMC, included in the DENIS catalogue. This classification is based on the fact that all stars brighter than the tip of the red giant branch must be AGB stars and in the colour–magnitude ( $I - J$ ,  $J$ ) diagram they are separated by a diagonal line from younger and foreground objects (Cioni, Habing & Israel 2000b).

A similar criterion was followed to identify AGBs in the colour–magnitude diagram ( $J - Ks$ ,  $Ks$ ), obtained with 2MASS (Skrutskie 1998) data. Cioni et al. (2006) identified a region in this diagram, enclosed by two lines, that should include the AGB stars in the sample (see equations 1 and 2 and fig. 1 in Cioni et al. 2006). The total sample was further split into O-rich and C-rich candidates; the two spectral classes were discriminated between by means of a straight line, the expression for which is given in equation (4) of Cioni et al. (2006).

A considerable step forward in the study of dust-obscured evolved stars in the LMC came with the data from IRAC and MIPS, mounted on board *Spitzer*. In particular, the SAGE Survey (Meixner et al. 2006) produced photometric data taken with IRAC for over six million stars. This allowed considerable progress in the study of

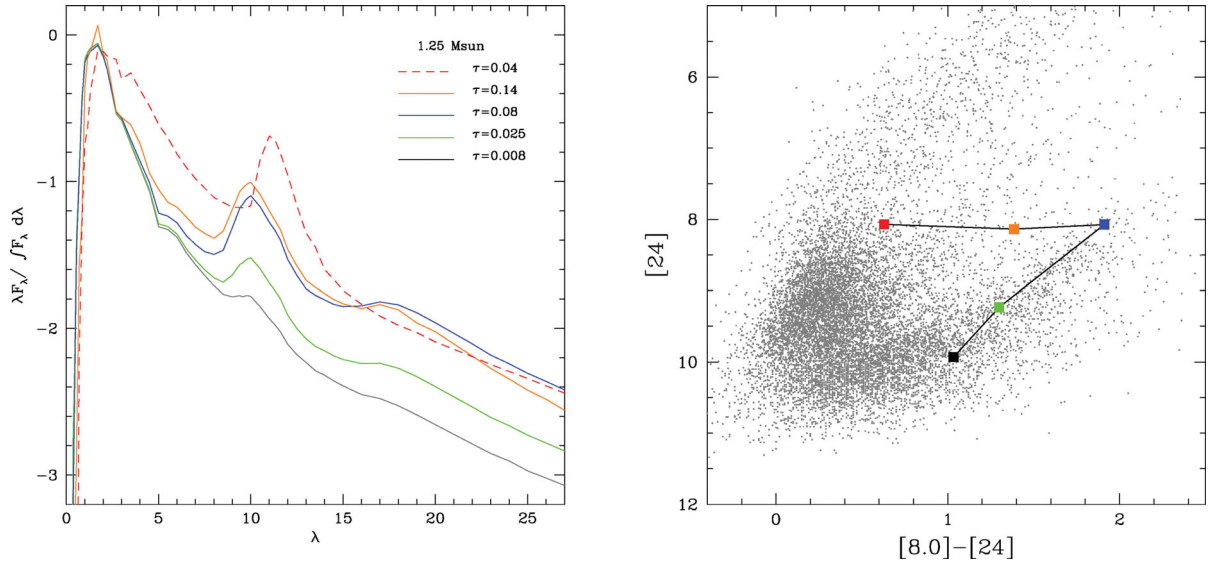


**Figure 9.** Left panel: the synthetic SED of a  $1.25 M_{\odot}$  model of metallicity  $Z = 8 \times 10^{-3}$  at various evolutionary stages. The O-rich phase of the star is represented with a solid line, while the dashed line refers to the C-rich stage. Right panel: the theoretical track in the  $[8.0] - [24]$  versus  $[24]$  colour–magnitude diagram, where the coloured points refer to the corresponding spectra in the left panel.

dust-enshrouded stars, because the IRAC and MIPS filters are centred in the spectral region where most of the emission from optically thick circumstellar envelopes occurs.

Blum et al. (2006), studying the obscured objects, identified a sequence of stars in the  $J - [3.6] > 3$  portion of the colour–magnitude ( $J - [3.6]$ ,  $[3.6]$ ) diagram that were classified as ‘extreme’ AGB stars (see fig. 3 of Blum et al. 2006).

The classification of LMC AGBs into C-rich and O-rich candidates, introduced by Cioni et al. (2006) and completed by the extreme stars of Blum et al. (2006), was subsequently used in all more recent investigations (Srinivasan et al. 2009, 2011; Riebel et al. 2010, 2012).

## 5.2 Our selection of the sample

We base our analysis on data available from the SAGE survey (Meixner et al. 2006), particularly the magnitudes in the 3.6-, 4.5-, 5.8- and 8.0- $\mu\text{m}$  IRAC bands and the 24- $\mu\text{m}$  MIPS band.

Riebel et al. (2010) extracted from the SAGE catalogue, containing  $\sim 6.5$  million sources, a list of  $\sim 30\,000$  evolved stars with high-quality infrared photometry,  $\sim 17\,000$  of which were classified as AGB stars. From this sample we selected the objects for which the 24- $\mu\text{m}$  flux is available, ruling out the sources for which  $[24] > 9.5$ . This choice allows a full statistical analysis, because the completeness of the data approaches 100 per cent at  $[24] = 9.5$ ; also, the  $3\sigma$  error in  $[8.0] - [24]$  is more than 0.5 mag above this limit (Sargent et al. 2011), rendering any comparison with observations unreliable. After the aforementioned cut at  $[24] < 9.5$ , we are left with a final sample consisting of  $\sim 6500$  stars. With this choice we exclude from our analysis the vast majority of low-luminosity, oxygen-rich stars present in the original sample by Riebel et al. (2010). However, accounting for these objects would add only a small contribution to the present investigation and, more importantly, their contribution to the overall dust production is expected to be low (below  $\sim 5$  per cent).

What makes the LMC an ideal target for studies of stellar populations is the high Galactic latitude, which minimizes the foreground

contamination. The analysis by Cioni et al. (2006) shows that the ( $J - K_s$ ,  $K_s$ ) criterion, adopted to select the AGB sample, is affected by very modest contamination by the Galaxy foreground. 2MASS selected sources probably include genuine RGB stars at the faintest magnitudes of M-type candidates (fig. 1 of Cioni et al. 2006); however, those sources are excluded from our selected sample, owing to the cut at  $[24] < 9.5$ .

Concerning distant objects, in the ( $J - [3.6]$ ,  $[3.6]$ ) diagram (see fig. 3 of Blum et al. 2006), the locus defined by the external galaxies does not overlap with the region occupied by AGBs. While distant galaxies are found at  $[3.6] > 12.5$ , AGBs populate the brighter part of the diagram in the regions at  $[3.6] < 12$ , thus preventing a relevant contamination by these objects. The detailed analysis by Boyer et al. (2011) shows that little contamination by foreground and background sources is expected for the AGB sample in the Magellanic Clouds (MCs), with contamination of the O-rich AGB sample estimated to be 2.5 per cent.

The reddest sources in our list overlap with the region of the CMD24 also populated by young stellar objects (YSOs). Whitney et al. (2008) isolated regions in the colour–magnitude ( $[8.0] - [24]$ ,  $[8.0]$ ) diagram expected to be populated by YSOs (see fig. 3 of their article). This separation includes a stringent cut at  $[8.0] - [24] = 2.2$  and  $[8.0] > 11 + 1.33 \times ([8.0] - [24])$ , to exclude AGB stars. We find that  $\sim 10$  sources in our catalogue occupy this region of the diagram, representing less than 0.3 per cent of our entire sample.

Riebel et al. (2010) classified AGB stars on the basis of their IR colours, dividing the total sample into ‘oxygen-rich’, ‘carbon-rich’ and ‘extreme’ objects. This classification was based on the prescriptions given by Cioni et al. (2006), discussed in the previous section. Among the stars from Riebel et al. (2010) included in our selected sample of  $\sim 6500$  objects, we find that 23 per cent are O-rich, 55 per cent are C-rich and 22 per cent are extreme stars. The relative fraction of O-rich stars is much smaller than in the original sample analysed by Riebel et al. (2010), because of our choice of focusing our attention on the sources with  $[24] < 9.5$ , thus ruling out many low-luminosity, oxygen-rich stars.

### 5.3 Synthetic diagrams in the *Spitzer* bands

The comparison between models and observations is based on an analysis of the CCD1, CCD2, CMD24 and CMD80 diagrams. This is the best choice to test our theoretical framework, because most of the emission from dust-enshrouded stars occurs in the infrared bands. The observed distribution of stars in the various diagrams is compared with synthetic diagrams obtained on the basis of our tracks.

To construct the synthetic diagrams, we used the SFH of the LMC given by Harris & Zaritsky (2009), which also provides the relative distribution of stars across the different metallicities, as shown in Fig. 4. In the present analysis we assume that the  $Z = 2.5 \times 10^{-3}$  stars share the same properties as their  $Z = 10^{-3}$  counterparts: we thus consider three metallicities, namely  $Z = 10^{-3}$ ,  $Z = 4 \times 10^{-3}$  and  $Z = 8 \times 10^{-3}$ .

We trace the history of the star formation rate and the stellar metallicities since the formation of the LMC, 15 Gyr ago. The time steps used are 10 Myr for the epoch ranging from 100 Myr ago until now, 100 Myr for the epoch going from 1 Gyr to 100 Myr ago and 1 Gyr for the epochs previous to 1 Gyr ago.

At each time step, we randomly extract a number of stars, distributed between the three metallicities considered, determined by the following factors: (i) the value of the star formation rate; (ii) the relative percentages of stars of different metallicities; (iii) the duration of the entire AGB phase of a star that has just completed the core helium-burning phase in the epoch considered. We used a Salpeter’s IMF, with index  $x = 2.3$ . The outcome of this work consists of a series of points extracted along the tracks of the various masses considered; for each point the infrared magnitudes are obtained by calculating a synthetic spectrum, as described in Section 2.3.

Fig. 10 shows the results of our simulations, with the expected distribution of stars in CCD1 (left panel) and CMD24 (right). Following the classification introduced in Section 4, we distinguish the stars according to the group they belong to: OCS, defined as the stars falling in region II in CCD1 (left panel of Fig. 10), HBBS,

populating region I in CCD1 (left panel of Fig. 10); FS stars, defined as the stars in the F zone of CMD24 (right panel of Fig. 10); CMS stars, defined as the objects in zone III in CCD1, not belonging to the FS group. In the same figure we also show the spectroscopically confirmed C stars of Gruendl et al. (2008), Zijlstra et al. (2006) and Woods et al. (2011) and O-rich sources from Sloan et al. (2008) and Woods et al. (2011).

The outcome of this synthetic approach is the simulation of the whole AGB sample in the LMC. However, coherently with the criterion for selecting the sample given in Section 5.2, we will use in the statistical analysis described in the following sections only the stars extracted with  $[24] < 9.5$ .

## 6 UNDERSTANDING THE OBSERVATIONS OF AGB STARS IN THE LMC

The analysis presented in this section is based on the comparison between observations of AGB stars in the LMC and the theoretical predictions obtained through the synthetic modelling described in the previous section.

Following the classification introduced in Section 4, we first compare the star counts in zones I, II, III and F shown in Figs 7, 8 and 10 with those observed. We check consistency among the number of objects in each group, by comparing the observed and expected distributions of colours and magnitudes.

The goal of the present analysis is twofold. On one hand we test the reliability of our theoretical understanding of the physics of AGBs, in terms of their evolutionary properties and the dust composition of their envelopes. At the same time, this approach allows a characterization of the stars observed, to determine their age, metallicity, surface chemical composition and dust present in their circumstellar envelope.

The results are shown in Table 2, where we report the observed and predicted fractions of stars in each group. The overall agreement is very good. For each of the four groups introduced in Section 4, Figs 11–14 show the comparison between the observed and

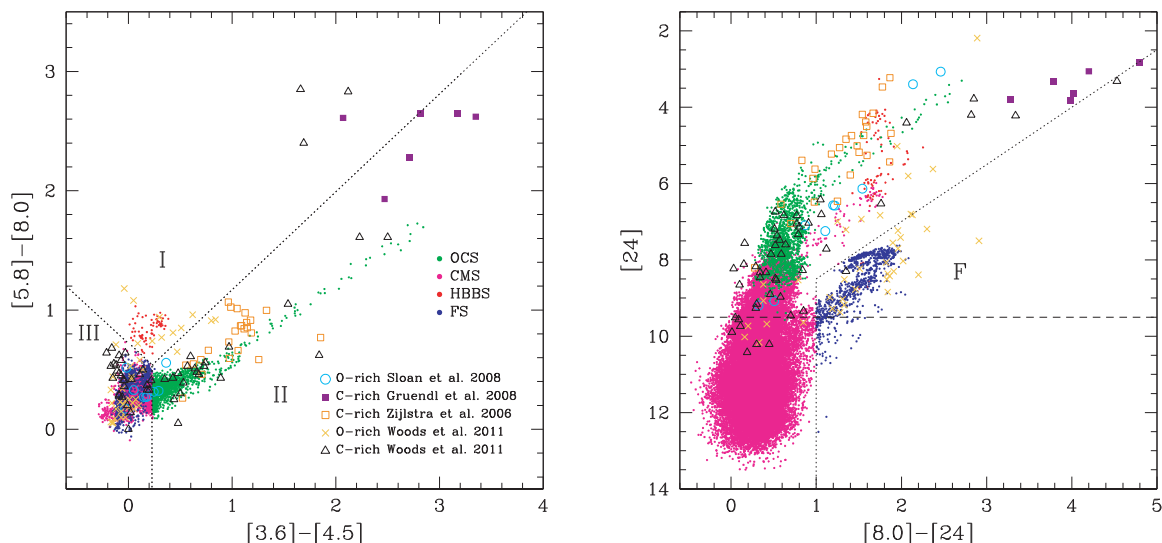


**Figure 10.** The distribution of the synthetic diagrams in the  $[3.6] - [4.5]$  versus  $[5.8] - [8.0]$  (left) and  $[8.0] - [24]$  versus  $[8.0]$  (right) planes. Spectroscopically confirmed C stars from Gruendl et al. (2008), Zijlstra et al. (2006) and Woods et al. (2011) are shown, overimposed to results from our simulation. The dotted line in the right panel represents the cut applied to the samples at  $[24] < 9.5$  to obtain a completeness of  $\sim 100$  per cent of data [A colour version of this figure is available in the online version, where stars belonging to each of the 4 groups introduced in Section 4 are shown with different colours: OCS (green), HBBS (orange), FS (blue), CMS (magenta)].

**Table 2.** Percentage of stars belonging to the four groups into which we divided the observed sample and the synthetic population of AGBs used in the present analysis (see the text in Section 4 for details).

	OCS	HBBS	FS	CMS
Observed	19	1	12	68
Expected	22	1	11	66

expected distribution of stars in the CCD1 (top left), CCD2 (top right), CMD24 (bottom left) and CMD80 (bottom right) diagrams. In each panel, we show the observed points present in the sample used here, extracted from Riebel et al. (2010), as black points. The stars from our simulation falling in each group are indicated with coloured points, using the same coding as in Fig. 10. For complete-

ness, we also show as grey points in Figs 11–14 all the stars in the original sample by Riebel et al. (2010).

We now discuss the stars in each group separately.

### 6.1 Obscured carbon stars

OCS are defined as the stars populating region II in CCD1, shown in Figs 7 and 10. In Fig. 11 we show the observed points belonging to this group in CCD1, CCD2, CMD24 and CMD80 as black dots; the stars from our simulations and classified as OCS are indicated in green. According to our modelling, no oxygen-rich star is expected to evolve into this region of CCD1 (see the left panels of Fig. 7), thus the OCS group is entirely composed of C stars. This is in agreement with the interpretation of the colour–colour  $[(3.6) - [4.5], [5.8] - [8.0)]$  diagram of the LMC given by Srinivasan et al. (2011) (see their fig. 7). The authors identified the stars in the diagonal band traced by OCS as carbon stars; sources with redder colours correspond to objects with larger optical depth.

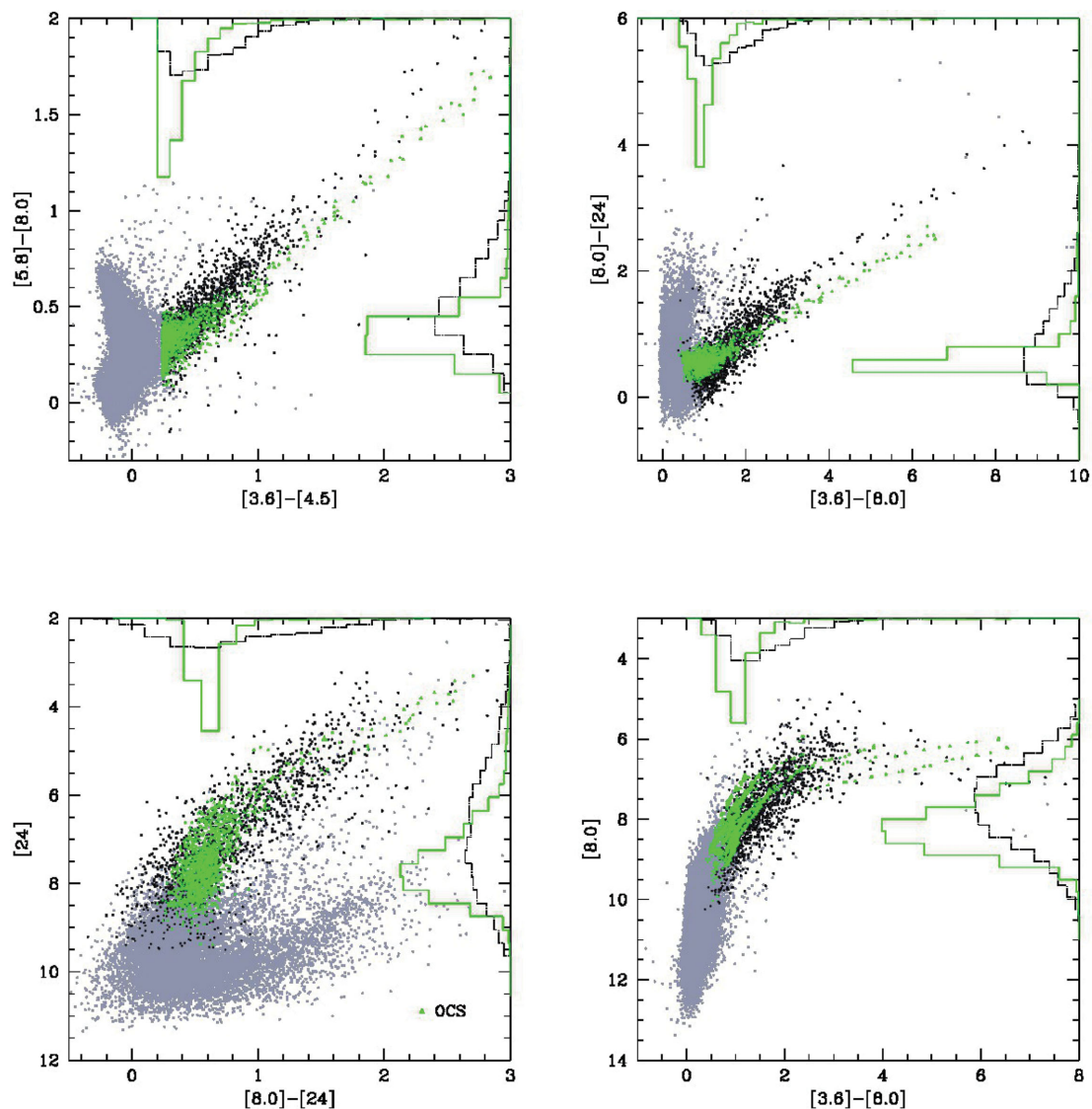


**Figure 11.** The distribution in the colour–colour  $[(3.6) - [4.5], [5.8] - [8.0)]$  (top left) and  $[(3.6) - [8.0], [8.0] - [24)]$  (top right) diagrams and in the colour–magnitude  $[(8.0) - [24], [24)]$  (bottom left),  $[(5.8) - [8.0], [8.0)]$  (bottom right) planes of the sample of OCS discussed in Section 6.1. The whole sample of stars by Riebel et al. (2012) is shown with light grey points; the black dots indicate the stars in the Riebel et al. (2012) sample that fall in region II of CCD1 and are thus classified as OCS according to the criteria given in Section 4. Full triangles (shown in green in the colour version of this figure, in the online version) indicate results from synthetic modelling. Note that the statistical analysis is limited to stars with  $[24] < 9.5$ .

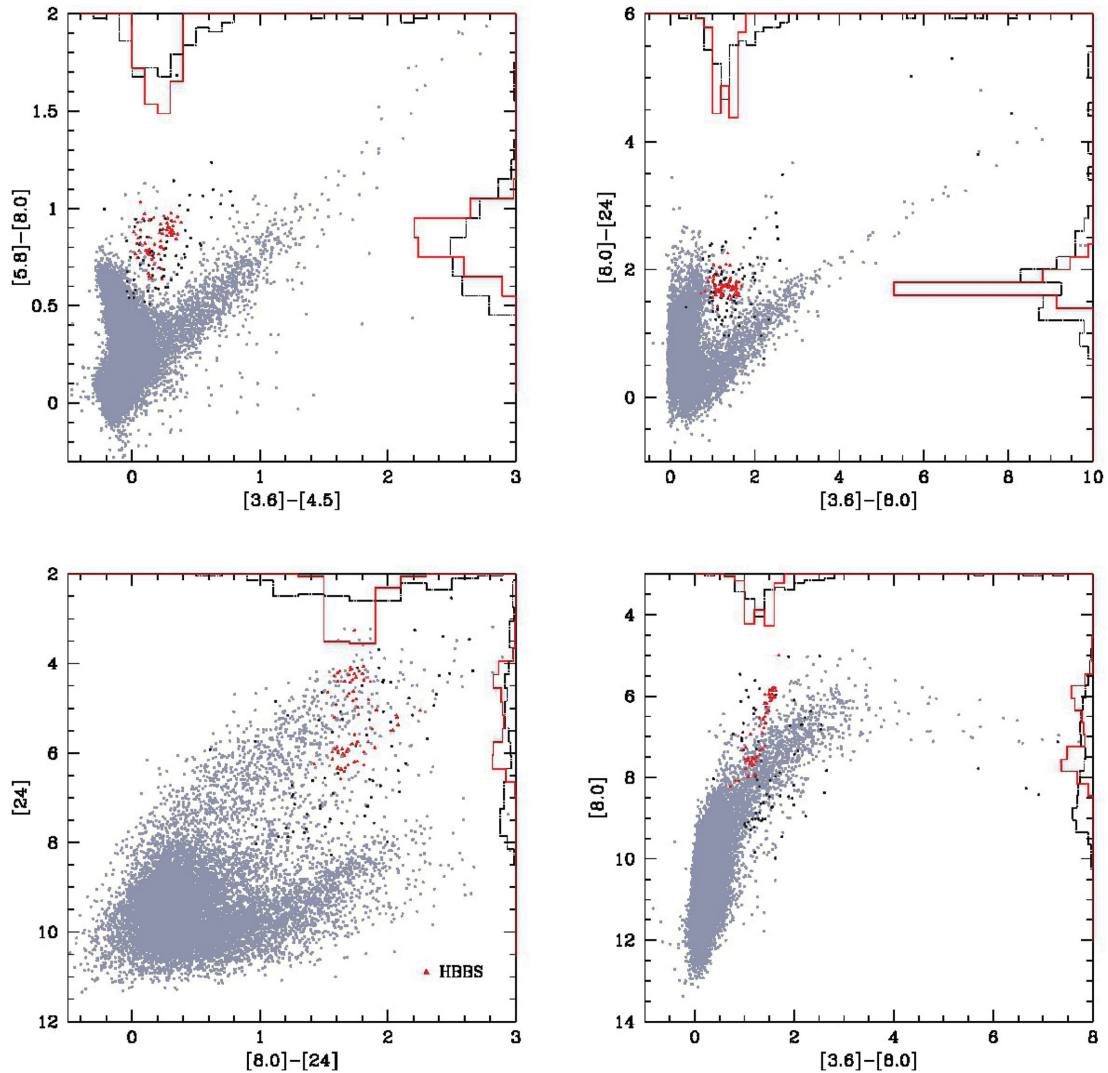


**Figure 12.** The same as Fig. 11, but for those stars classified as HBBS in Section 4. The results from synthetic modelling are indicated as full triangles (shown in red in the colour version of this figure is available in the online version).

In CCD1, OCS trace a diagonal band, with  $0.2 < [3.6] - [4.5] < 3$ ,  $0.2 < [5.8] - [8.0] < 1.6$ . The optical depth increases along this sequence, ranging from  $\tau_{10} = 0.01$  for the least obscured dust objects, at  $[3.6] - [4.5] \sim 0.2$ , to  $\tau_{10} = 3.5$  for the stars surrounded by optically thick envelopes, with  $[3.6] - [4.5] \sim 3$ . A similar behaviour is followed in CCD2, with  $[3.6] - [8.0]$  ranging from  $\sim 0.5$  to  $[3.6] - [8.0] \sim 7$ .

Based on the arguments discussed in Section 3.2, we interpret OCS as an evolutionary sequence. Once they achieve the carbon-star stage, the stars become progressively more obscured and reddened (see the dashed lines in Fig. 5), because (i) as a consequence of repeated TDU episodes, the surface carbon abundance increases (see Fig. 2), thus increasing the density of carbon molecules available for condensation, and (ii) the increase in carbon leads to cooler temperatures (Marigo 2002), which makes the dust formation region closer to the surface of the star, in higher density regions.

The evolution of the amount of dust formed around C-rich AGBs and the sequence of the different dust layers present are discussed in detail in previous articles by our group (see e.g. Ventura et al. 2014a), where the interested reader can also find a detailed discussion on the size of particles of individual species present in the circumstellar

envelope (see in particular fig. 5 in Ventura et al. 2014a and fig. 1 in Dell’Agli et al. 2014a). These stars are surrounded by two dusty layers: (i) a more internal region,  $\sim 2$  stellar radii away from the surface of the star, with SiC grains of  $\sim 0.05\text{--}0.08 \mu\text{m}$  size<sup>4</sup> and (ii) a more external zone,  $\sim 5R_*$  from the surface, with SiC and solid carbon particles. The latter grains determine most of the obscuration of the radiation coming from the star; their dimension ranges from  $\sim 0.05 \mu\text{m}$  in the less obscured OCS ( $0.01 < \tau_{10} < 0.1$ ) up to  $\sim 0.2 \mu\text{m}$  in the most heavily dust-obscured objects ( $\tau_{10} > 3$ ) (Nanni et al. 2013b; Ventura et al. 2014a).

The progenitors of OCS are stars of initial mass in the range  $1 M_{\odot} < M \leq 3 M_{\odot}$ , formed  $3 \times 10^8\text{--}3 \times 10^9$  years ago (see Table 1). Younger (and more massive) objects experience HBB, thus not reaching the C-star stage. The left panel of Fig. 15 shows the predicted distribution of OCS in terms of the initial mass and metallicity of the progenitors. The majority of OCS are the

<sup>4</sup> These results depends on the metallicity, because the abundance of the key element to form SiC, i.e. silicon, scales with  $Z$  (Nanni et al. 2013b; Ventura et al. 2014a).

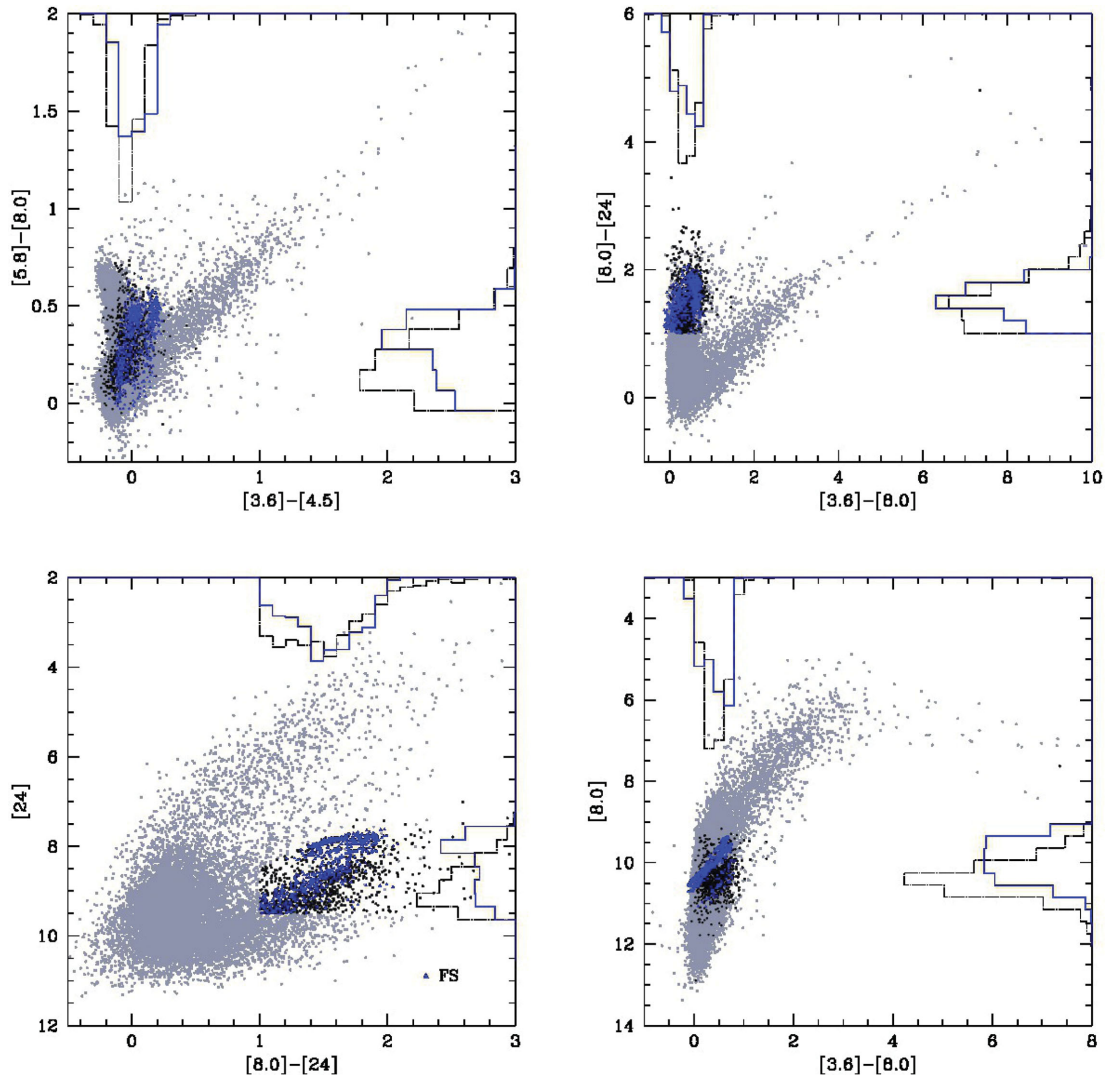


**Figure 13.** The same as Fig. 11, for the FS stars populating the finger identified by Blum et al. (2006). The models are indicated with full triangles (see the colour version of this figure is available in the online version, where the models are indicated in blue).

descendants of low-mass stars with masses  $M \sim 1\text{--}2 M_{\odot}$ , formed during the burst of SFH in the LMC that occurred  $\sim 2$  Gyr ago (Harris & Zaritsky 2009). These objects are mainly low-metallicity ( $Z$  below  $4 \times 10^{-3}$ ) stars, which spend  $\sim 70$  per cent of their AGB lifetime as carbon stars (see the right panel of Fig. 2). A non-negligible tail ( $\sim 10$  per cent of the total number of stars extracted, classified as OCS) of higher- $Z$  ( $Z > 4 \times 10^{-3}$ ) stars of mass  $2 M_{\odot} \leq M \leq 3 M_{\odot}$  is evident in Fig. 15. The latter group of stars are the descendants of objects formed during the peak in the SFH occurring  $\sim 5 \times 10^8$  year ago (see Table 1 for the evolutionary time-scales of the individual masses), when the majority of the stars have metallicity  $Z > 4 \times 10^{-3}$ , as shown in Fig. 4 (Harris & Zaritsky 2009).

Though smaller in number, this group of more massive OCS of metallicity  $Z \geq 4 \times 10^{-3}$  plays a relevant role in the interpretation of the observed CCD1 and CCD2, as they are the only stars expected to evolve redder than  $[3.6] - [4.5] > 1$  and  $[3.6] - [8.0] > 2.5$  (see the left and middle panels of Fig. 5). We will refer to these models as extremely obscured carbon stars (EOCS). The reason for this is twofold: (i) stars more massive than  $\sim 2 M_{\odot}$  experience a high number of TDU episodes, thus they accumulate great quantities of carbon in the surface regions, which reflects in a high-efficiency

formation of solid carbon particles and (ii) as shown in Fig. 2, the degree of obscuration reached by lower- $Z$  models is smaller, because they evolve at larger surface temperatures, which causes the dusty layer to form at larger distances and smaller densities. The evident decrease in the number of stars in the reddest portion of CCD1 and CCD2 (populated by the EOCS) is partly due to the fact that only a limited range of masses of the more metal-rich component is expected to evolve in those zones of the planes; a further reason is the short duration of the most obscured phase (Fig. 5), a consequence of the strong increase in the rate of mass loss during these evolutionary stages.

An obvious difference in the dust composition between models of different metallicity is the quantity and size of SiC grains formed. In the  $Z = 10^{-3}$  case, owing to the scarcity of silicon, the formation of SiC (if any) is extremely modest, whereas in stars with  $Z = 4 - 8 \times 10^{-3}$  the contribution of SiC to the thermal emission of dust (which can be expressed via the optical depth  $\tau_{10}$ ) is far from being negligible. The silicon available at the surface of the star is less than the carbon, thus solid carbon is produced in larger quantities than SiC; however, SiC particles form closer to the surface of the star, in a relatively higher temperature region, thus providing an

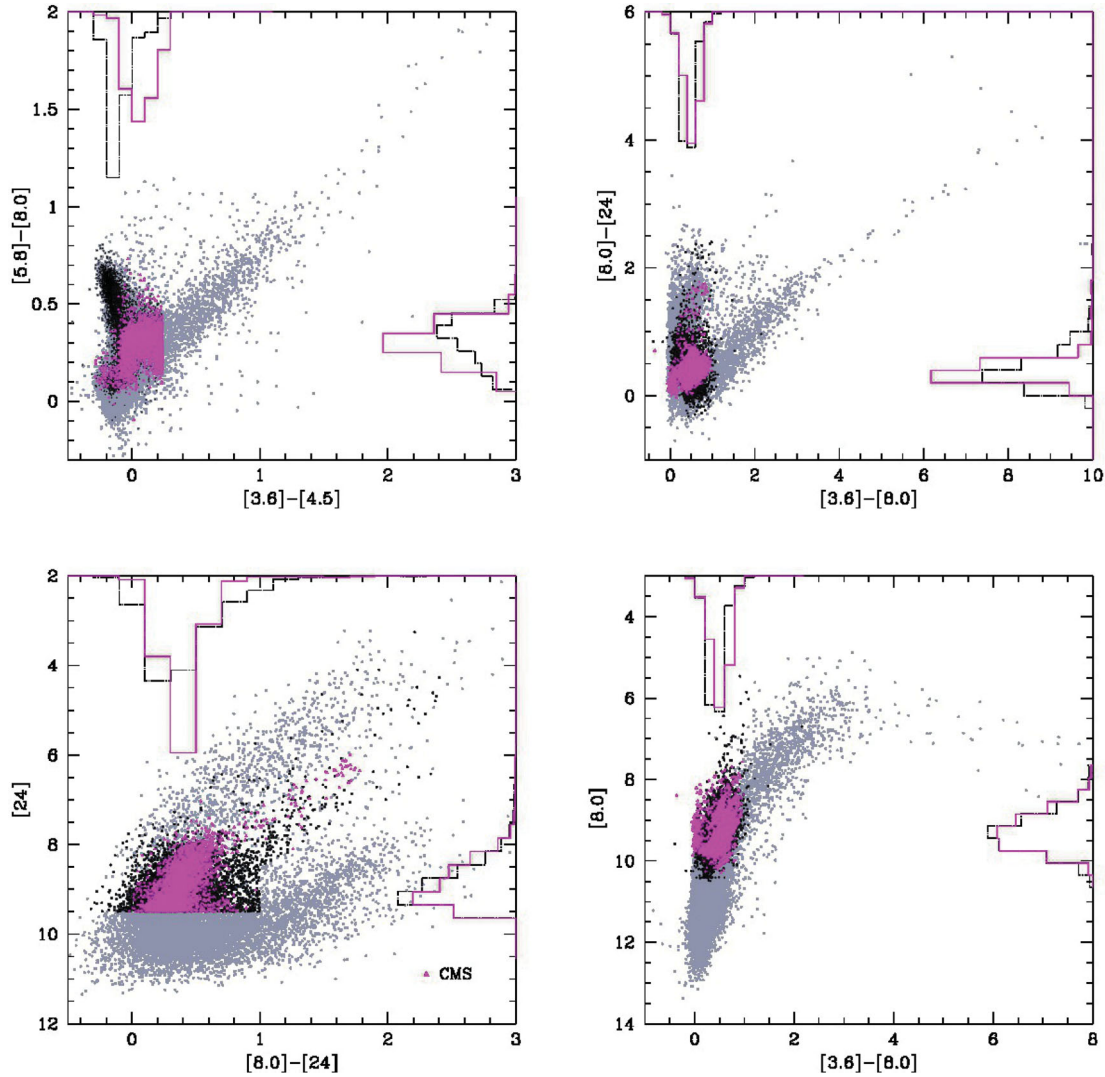


**Figure 14.** The distribution in the colour–colour and colour–magnitude diagrams of the stars classified as CMS in Section 4. Results from synthetic modelling are also shown (these points are shown in magenta in the see the colour version of this figure is available in the online version).

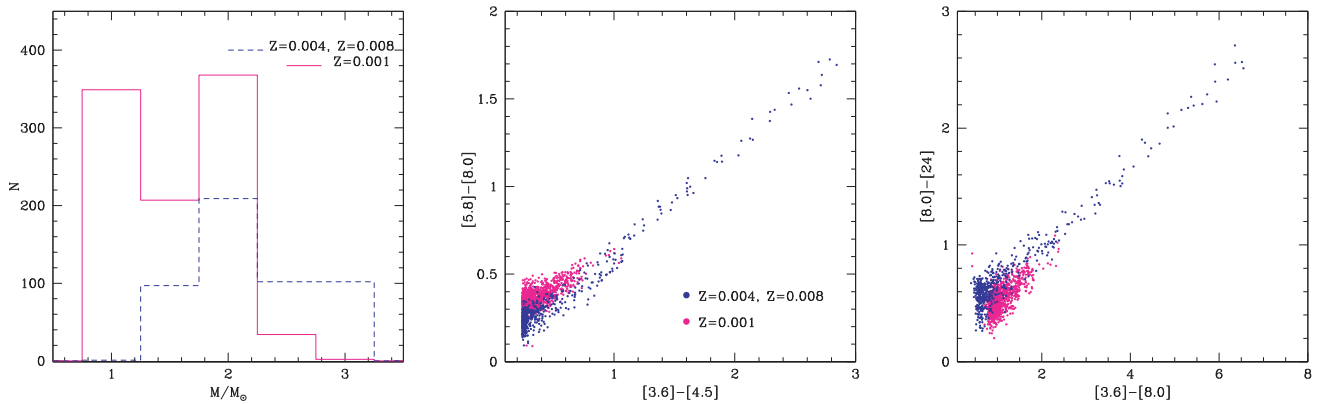


**Figure 15.** Left panel: the distribution of OCS in terms of initial mass and metallicity. The solid line (shown in magenta in the colour version of this figure is available in the online version) refers to  $Z = 10^{-3}$ , while the dashed line (shown in blue in the online version) represents  $Z \geq 10^{-3}$ . Middle and right panels: the expected population of dust-obscured, C-rich stars in the colour–colour ( $[3.6] - [4.5]$ ,  $[5.8] - [8.0]$ ) (middle) and ( $[3.6] - [8.0]$ ,  $[8.0] - [24]$ ) (right) planes (see the colour version of this figure is available in the online version, where the  $Z = 10^{-3}$  population are indicated in magenta, whereas the  $Z = 4-8 \times 10^{-3}$  stars are indicated in blue).

important contribution to  $\tau_{10}$ . The variation in the SiC/C ratio is the reason for the spread in the observed  $[5.8] - [8.0]$  colours of OCS in region  $[3.6] - [4.5] < 1$  of CCD1. This observational evidence (see e.g. the top left panel of Fig. 11) is confirmed by our simulations. The middle panel of Fig. 15 shows the metal distribution of stars in this zone of CCD1, determined by our synthetic modelling. This plot shows that, for a given  $[3.6] - [4.5]$ , low-metallicity stars assume redder  $[5.8] - [8.0]$  colours, while more metal-rich objects populate the lower portion of CCD1. Looking at the theoretical tracks in this plane, shown in the left panels of Fig. 7, we see that the latter region of CCD1 is reproduced by the track of low-mass stars belonging to the more metal-rich population, in the phases following the beginning of the carbon-star phase. Spectral observations of carbon stars located in magenta regions will find a weaker SiC feature, compared with the blue region with  $[3.6] - [4.5] < 1$ . The spread in the observed sequence of OCS vanishes for  $[3.6] - [4.5] > 1$ : as shown in Fig. 7, this stems from the lack of metal-poor stars in this zone of CCD1, which is populated only by stars of metallicity  $Z \geq 4 \times 10^{-3}$  (compare the tracks of the  $Z = 10^{-3}$  and  $Z = 8 \times 10^{-3}$  models in the left panels of Fig. 7).

The situation in CCD2 is similar: the diagonal band traced by OCS in this plane exhibits an intrinsic width that becomes progressively smaller for  $[3.6] - [8.0] > 3.5$ . The right panel of Fig. 15 shows that even in this case the spread is associated with the metal content of the star, metal-rich objects populating the upper side of CCD2.

Among the stars in the sample defined in Section 5.2, 22 per cent are found to be in region II in CCD1 as shown in the left panels of Fig. 7, which according to our interpretation is populated by OCS. This is in nice agreement with our prediction (20 per cent, see Table 2), confirming that the overall duration of the C-rich phase for the masses involved in this process is predicted well by our models. In terms of the colour distribution of the OCS, we see in the top left and top right panels of Fig. 11 that our distribution of OCS is excessively peaked towards the less dust-obscured objects, indicating that the transition to the highly obscured phase is too slow. This is presumably due to the large sensitivity of the effective temperature of the mass-loss rate adopted (Wachter et al. 2002, 2008), which causes the whole residual envelope to be lost rapidly as the external regions of the star become carbon-rich, possibly indicating the need for a softer dependence of  $\dot{M}$  on  $T_{\text{eff}}$ .

In the CMDs shown in Fig. 11 (bottom panels), the OCS trace a diagonal band, which, consistent with their distribution in the CCDs, can be interpreted as an evolutionary sequence towards higher degrees of obscuration. During the carbon-rich phase, the total luminosity changes little at a given initial mass (see middle panel of Fig. 1 of Dell’Agli et al. 2014a). Hence, the increase of the 8.0- and 24- $\mu\text{m}$  flux is not due to an increase in luminosity, but rather an increase in dust optical depth, which makes the absorption of optical and near-infrared photons emitted by stars and the re-emission at mid-infrared wavelengths more efficient.

Unlike CCD1 and CCD2, in the CMD24 plane the OCS population is partially overlapped with the bright oxygen-rich stars, thus inhibiting the possibility of discrimination between the two samples. This can be seen by comparison of the position of OCS and HBBS in the CMD24 plane, shown, respectively, in the bottom left panels of Figs 11 and 12. The tracks of OCS and HBBS shown in the left panels of Fig. 8 support this conclusion further.

As shown in the bottom right panels of Figs 11 and 12 and confirmed by the tracks shown in the right panels of Fig. 8, the situation is more clear in CMD80, where the two sequences are separated. The observations show that the majority of stars with

$[3.6] - [8.0] > 1.5$ ,  $[8.0] < 8$  are carbon stars (Matsuura et al. 2009; Woods et al. 2011) and we agree that this region is occupied mainly by high mass-loss rate C stars. Indeed, we see in Fig. 10 that our OCS models nicely fit the position of spectroscopically identified carbon-rich stars sampled by Zijlstra et al. (2006) in CCD1 and CMD24. The same models also reproduce the IR colours of the C-rich sample by Woods et al. (2011). However, a few stars belonging to the sample by Gruendl et al. (2008) and Woods et al. (2011) are barely reproduced by our models: this suggests a need for an improvement in the description of the star+dust systems of C-rich stars in the very latest evolutionary phases. OCS constitute the vast majority of dust-obscured stars in the CMD24 and CMD80 planes, in the regions  $[8.0] < 8$  and  $[24] < 6$ ; this is evident in the distribution of stars in Fig. 11.

Concerning the distribution between the various metallicities, we find that, similarly to CCD1 and CCD2, only metal-rich stars evolve to the redder regions of CMD24 and CMD80, as can be seen in Fig. 8, showing the evolutionary tracks in these planes. We identify the two regions with  $[3.6] - [8.0] > 2$  and  $[8.0] - [24] > 1$  as populated by the most obscured OCS belonging to the more metal-rich populations.

## 6.2 Stars experiencing hot bottom burning

In Section 4, we defined HBBS as the stars in region I in CCD1, shown in Fig. 7. This zone is populated by a group of stars clustering around  $[3.6] - [4.5] \sim 0.2$ ,  $[5.8] - [8.0] \sim 0.8$ , detached from the rest of the LMC population of AGBs. The observed stars falling in the HBBS region are shown with black dots in Fig. 12; full triangles indicate results from our simulation. We interpret these sources (see the tracks shown in Fig. 7) as the descendants of massive AGBs with mass initially above  $3 M_{\odot}$ , experiencing strong HBB at the base of the convective envelope. According to the arguments presented in Section 2.2, the circumstellar envelope of HBBS hosts a more internal ( $\sim 2R_*$  away from the surface of the star), largely transparent zone populated by alumina grains and a more external region,  $\sim 10R_*$  far from the surface, where silicates grains form and grow. The latter dust species is the most relevant in determining the degree of obscuration of the star.

The occurrence and strength of HBB is the key quantity to determine the amount of silicates formed. The degree of obscuration is considerably smaller than for their C-rich counterparts ( $\tau_{10}$  is below 2 in all cases): this difference stems from the much higher availability of carbon molecules in the envelope of carbon stars, compared with the abundance of silicon in the outer regions of oxygen-rich stars.

We see in the left panels of Fig. 7 that the theoretical tracks of HBBS in CCD1 and CCD2 are more vertical than those of OCS. In CCD1, the reason is the prominent silicate feature at  $\sim 9.7 \mu\text{m}$ , which determines an increase in the  $\sim 8.0\text{-}\mu\text{m}$  flux, thus rendering the  $[5.8] - [8.0]$  colour extremely red. This effect is clearly evident in the middle panel of Fig. 5, showing that, in comparison with C stars, oxygen-rich stars experiencing HBB evolve at redder  $[5.8] - [8.0]$ , which reaches the highest values once strong HBB conditions are experienced. Concerning CCD2, the higher slope of the tracks of HBBS compared with OCS stems from the optical properties of silicates, which reprocess the radiation emitted from the central star, with substantial emission at mid-infrared wavelengths.

HBBS formed during the burst in the SFH in the LMC occurring  $\sim 10^8$  years ago, as shown in Fig. 4. These sources descend from

stars with initial mass in the range  $3.5 M_{\odot} \leq M \leq 7.5 M_{\odot}$ .<sup>5</sup> They belong to the more metal-rich population, because of the small percentage of low- $Z$  stars formed during these epochs (Harris & Zaritsky 2009). Also, stars of  $Z < 4 \times 10^{-3}$ , with the exception of massive SAGBs, produce only a modest quantity of dust (Ventura et al. 2012b), thus they are not expected to evolve into the region in the CCD1 plane (region I in the left panels of Fig. 7) populated by HBBS (see the bottom left panel of Fig. 7).

The paucity of objects in the HBBS region (they account for  $\sim 1$  per cent of the total sample, see Table 2) not only stems from the intrinsically small number of stars formed in the relevant range of mass, but also is a consequence of HBB: as shown in Fig. 1, HBB produces a fast increase in the luminosity of the star, which, in turn, favours a rapid loss of the residual external mantle. The limitation of the HBBS population to the metal-rich component is a further reason for the small number of HBBS observed.

In the colour–magnitude ([3.6] – [8.0], [8.0]) diagram (see the bottom right panels of Figs 11 and 12), HBBS define an almost vertical sequence, separated from OCS. The reason is once more the silicate feature, which renders the [8.0]- $\mu\text{m}$  flux of HBBS brighter than OCS at a given [3.6] – [8.0]. The observations have shown that high mass-loss rate oxygen-rich AGB stars, though in the minority in number, contaminate the region [3.6] – [8.0] > 1.5, [8.0] < 8 (Matsuura et al. 2009; Woods et al. 2011). Our models do not predict such a population, indicating that the excursion of the theoretical tracks in this plane is too vertical, with no bending towards redder [3.6] – [8.0] colours. Our massive AGB models experience large mass-loss rates, strongly favouring the formation of silicates. We therefore rule out the suggestion that this effect originates from the description of the AGB evolution. The discrepancy between observations and theoretical predictions suggests a problem in the shape of the synthetic spectra in the region of the silicate feature, which would affect the theoretical [8.0]- $\mu\text{m}$  flux. More detailed explorations, using different set of the optical constants of silicates, are needed to confirm this hypothesis.

The same separation between OCS and HBBS is not clear in the ([8.0] – [24], [24]) plane, as can be seen in the bottom left panels of Figs 11 and 12.

As shown in Fig. 10, by looking at the theoretical distribution of stars in the CCD1 and CMD24 planes, a fraction of the AGB stars spectroscopically classified as O-rich in the sample by Woods et al. (2011) show similar colours to the HBBS population. Sargent et al. (2011) suggested that obscured oxygen-rich stars populate the region in CCD1 at [3.6] – [4.5]  $\sim 0.2 - 0.3$ , [5.8] – [8.0]  $\sim 0.8 - 1$ , where, according to our interpretation, stars experiencing HBB should evolve (see their fig. 5). In their analysis, the authors presented a wide exploration of the various parameters relevant for the determination of the infrared colours (effective temperature, optical depth, inner border of the dusty region, etc.): the grid of models for oxygen-rich stars was shown first to extend in the direction of redder [3.6] – [4.5] and [5.8] – [8.0], then, after reaching the position occupied by HBBS, to turn to much redder [3.6] – [4.5], with [5.8] – [8.0] becoming bluer (see fig. 5 in Sargent et al. 2011).

<sup>5</sup> The strength of HBB experienced by intermediate-mass AGBs is extremely sensitive to the convection model used Ventura & D’Antona (2005). The models presented in this work are based on the FST treatment, which favours strong HBB in all stars more massive than  $\sim 3 M_{\odot}$ . In AGB models based on the traditional mixing-length theory, HBB is found in a narrower range of masses (see the detailed discussion in Ventura et al. (2013) on this argument).

Our theoretical sequences of oxygen-rich stars experiencing HBB follow a similar path (see the track corresponding to the  $5.5 M_{\odot}$  model in the left panel of Fig. 7); however, our models do not extend beyond the HBBS zone, because we find  $\tau_{10} < 2$  in all cases, at odds with Sargent et al. (2011), who explored the range  $10^{-4} < \tau_{10} < 26$ .

Concerning the interpretation of the CMDs, we stress that for HBBS, unlike OCS, the spread in the 8.0- and 24- $\mu\text{m}$  fluxes partly reflects a difference in the overall luminosity of the stars observed (see Fig. 1). The HBBS on the upper side of the two CMDs ([8.0] and [24]  $\sim 6$ ) correspond to the more massive stars ( $M \sim 5-6 M_{\odot}$ ) experiencing the strongest HBB, with scarce contamination from TDU. This offers the opportunity of testing this interpretation observationally, because these sources should show the typical signatures of proton capture nucleosynthesis, with  $^{13}\text{C}/^{12}\text{C} \sim 0.3$  and  $\text{C}/\text{N} \sim 0.02-0.03$ . This test could also be used to distinguish massive AGBs from red supergiant stars, which occupy the same regions in CMD24 and CMD80. The use of lithium is not straightforward in this context, because the lithium-rich phase is rapidly terminated once  $^3\text{He}$  is consumed in the envelope (Sackmann & Boothroyd 1992; Mazzitelli, D’Antona & Ventura 1999).

### 6.3 Stars in the ‘finger’ identified by Blum et al. (2006)

In an article focused on the infrared colour–magnitude diagrams of evolved stars in the LMC, Blum et al. (2006) noticed in the colour–magnitude ([8.0] – [24], [24]) diagram a sequence of O-rich candidates defining a prominent finger, spanning a range of 24- $\mu\text{m}$  excess of  $\sim 2$  mag. These stars, shown with full dots in Fig. 13, were identified by the authors as a faint population of dusty sources with significant mass loss.

We refer to this group of stars, populating region F (here we use the original definition by Blum et al. 2006) in the left panels of Fig. 8, as FS. According to our interpretation, this region is populated by low-mass  $M$  stars, with metallicity in the range  $4 \times 10^{-3} < Z < 8 \times 10^{-3}$ , of initial mass slightly above  $1 M_{\odot}$ , in the AGB phases immediately before becoming C stars. The track of a  $M = 1.25 M_{\odot}$  model of metallicity  $Z = 8 \times 10^{-3}$ , evolving into the F region, is shown as a black line in the top left panel of Fig. 8. The evolution of the same  $1.25 M_{\odot}$  model, in terms of the excursion of the evolutionary track in CMD24 and the SED at some selected evolutionary phases, is shown in Fig. 9. The initial excursion to the red, shown in the right panel of Fig. 9, is due to the larger and larger quantities of dust produced in the circumstellar envelope, while the following turn to the blue, at [8.0] – [24]  $\sim 1.8$ , coincides with the beginning of the C-star phase. CMD24 is by definition the best plane where the FS population can be distinguished from the other AGBs in the sample used here. However, inspection of Figs 11–14 suggests that in the CCD2 plane FS also populate a well-identified, almost vertical region, with no OCS and HBBS and with a limited number of CMS (see next section). In CCD1 and CMD80, FS are overlapped to the CMS stars, which will be discussed in the following section.

FS are the descendants of low-mass ( $M \leq 1.5 M_{\odot}$ ) stars with metallicity  $Z \geq 4 \times 10^{-3}$ , formed a few Gyr ago; in the bottom left panel of Fig. 8 we see that metal-poor objects do not evolve into the F region, owing to the small amount of silicate dust formed in their surroundings. The nice agreement between the predicted and observed number of FS stars (see Table 2) confirms the relative duration of the O-rich phase in these low-mass models and also the total duration of the AGB phase once they reach the C-star stage. Comparison with the observations in Fig. 10 shows that our models of FS stars fit nicely the position of a fraction of AGB

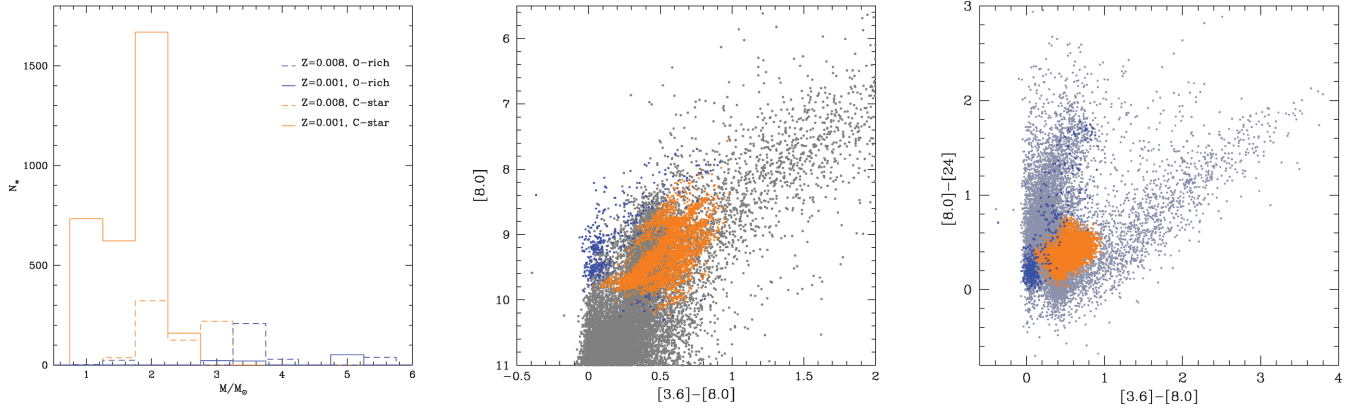


**Figure 16.** Left: the distribution of CMS in terms of initial mass and metallicity (dashed line for  $Z = 8 \times 10^{-3}$  and solid line for  $Z = 10^{-3}$ ), divided into O-rich and C-stars (in the colour version of the figure, available in the on line version, these two groups are indicated, respectively, with blue and orange lines). Middle: the expected population of CMS in the  $[3.6] - [8.0]$  versus  $[8.0]$  plane (see the online version, where the O-rich and C-rich population in the middle panel are indicated, respectively, with blue and orange points.) Right: the CMS population in the colour-colour  $([3.6] - [8.0], [8.0] - [24])$  diagram, with the division between carbon and oxygen stars.

stars in the sample by Woods et al. (2011), classified as O-rich, in the CMD24 plane. A word of caution is needed here. While these results, particularly the relative number of FS stars and the reddest points reached in the  $([8.0] - [24], [24])$  plane during their evolution, can be used to confirm further the reliability of the AGB models, the same does not hold for the description of the dust formation process. Unlike the cases examined so far, here the wind is not expected to suffer great acceleration under the effects of radiation pressure acting on dust particles; this renders the results partly dependent on the assumptions concerning the initial velocity with which gas particles enter the condensation zone.

On the side of the surface elemental abundance, we expect that these stars reflect substantially the initial composition of the gas from which they formed, considering that neither TDU nor HBB modified their composition. Only a slight increase in the helium and nitrogen content and a decrease in the carbon mass fraction are expected, as a consequence of the first dredge-up.

#### 6.4 Scarcely dust-obscured objects

The last group of objects considered are those in the *Spitzer* catalogue populating region III in CCD1 (see the left panels of Figs 7 and 10); because this region is also populated by FS stars, the latter have been subtracted in the identification of this sample. Clearly the statistical analysis will be restricted to sources with  $[24] < 9.5$ , in agreement with the definition of the AGB sample used in this work, specified in Section 5.2.

This subsample accounts for  $\sim 65$  per cent of the entire population (see Table 2); it is made up of both carbon and oxygen-rich stars (CMS), with a modest degree of obscuration. Our models indicate that the optical depth  $\tau_{10}$  is generally below 0.01, reaching  $\tau_{10} = 0.1$  in a limited number of cases. In the colour-magnitude diagrams shown in the bottom panels of Fig. 14, they are within the regions with  $8 < [8.0] < 10$  and  $7.5 < [24] < 9.5$ .<sup>6</sup> The agreement between observations and predictions is once more satisfactory in these planes.

According to our analysis, the majority of CMS are low-metallicity models with initial mass in the range  $1-2 M_{\odot}$ . This is

represented in the left panel of Fig. 16, showing the mass and metallicity distribution of CMS.  $\sim 90$  per cent of this sample is made up of carbon stars, either with a small C/O ratio or in the phases immediately following the extinction of TPs. The remaining  $\sim 10$  per cent are oxygen-rich stars, mainly low-mass objects in the early AGB phases, when they are still oxygen-rich; a limited number of more massive sources in the phases before the activation of HBB is also expected.

The relative fraction of stars in the observed sample used here belonging to the CMS group is found to be in nice agreement with the expected percentage of CMS, as indicated in Table 2. This indicates that the duration of the various evolutionary phases obtained via the theoretical models is consistent with the observational picture.

Compared with observations of spectroscopically confirmed stars, we see in Fig. 10 that our models of CMS explain the IR colours in the CCD1 and CMD24 diagrams of O-rich stars by Sloan et al. (2008) and of some C-rich stars by Woods et al. (2011).

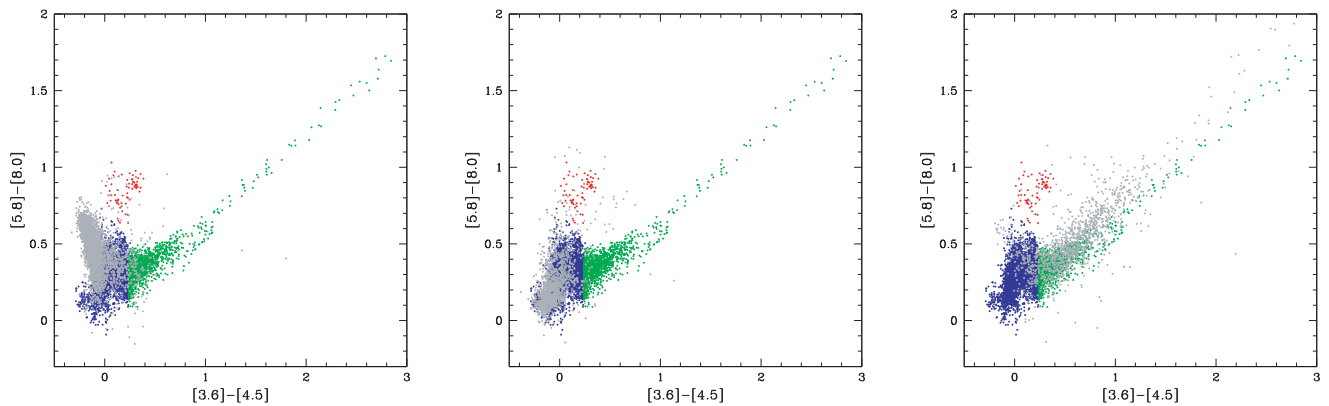
In CMD2, the position of the points from our simulation fits the observed distribution nicely, as shown in the top right panel of Fig. 14. A few CMS populate the region  $1 < [8.0] - [24] < 2$ , mainly occupied by FS (see top right panel of Fig. 13). Concerning CCD1, we note that the observed distribution of colours of CMS is not fully reproduced by the models: in particular, a group of stars in the region around  $[3.6] - [4.5] \sim -0.2$ ,  $[5.8] - [8.0] \sim 0.6$  is out of the range covered by the theoretical tracks (see top left panel of Fig. 14).

We identify most of these stars as carbon-rich ( $C/O > 3$ ) objects not heavily obscured in the phases immediately following the TP, before dust is produced in great quantities: as a consequence, the synthetic spectra are essentially determined by the spectrum of the central star, barely modified by the optically thin envelope. No influence of the dust formation scheme is expected here. We note that the same problem in reproducing the position of these stars in CCD1 was already found by Srinivasan et al. (2011) (see their fig. 7 and the discussion in section 4.2.5). Note that a few stars from the O-rich sample by Woods et al. (2011) fall in this region of CCD1. Both the theoretical tracks presented in Figs 7 and 8 and the spectroscopically confirmed objects in Fig. 10 show that the distribution of M stars and C-rich objects in the CMS sample overlaps in the CCD1 and CMD24 planes, thus preventing the possibility of disentangling the two populations. Conversely,

<sup>6</sup> The upper limits given above depend on our choice to limit this investigation to stars observed at  $[24] < 9.5$ .

**Table 3.** Main properties of dust-obscured AGBs in the LMC.

Class	$Z$	Age (Gyr)	$M/M_{\odot}$	$\tau_{10}$	Dust (size)	Surface elemental abundance
OCS extreme (95 per cent), C (5 per cent)	$10^{-3}$ (70 per cent) $4-8 \times 10^{-3}$ (30 per cent)	0.4–3	1–3	0.02–1	C (0.07–0.15 $\mu\text{m}$ ) SiC (< 0.08 $\mu\text{m}$ )	$10^{-3} < X(\text{C}) < 0.03$ $3 \times 10^{-5} < X(\text{N}) < 10^{-3}$ $5 \times 10^{-4} < X(\text{O}) < 5 \times 10^{-3}$
EOCS extreme	$4-8 \times 10^{-3}$	0.5	2.5–3	1–3	C (0.15–0.25 $\mu\text{m}$ ) SiC (0.08 $\mu\text{m}$ )	$5 \times 10^{-3} < X(\text{C}) < 0.015$ $4 \times 10^{-4} < X(\text{N}) < 8 \times 10^{-4}$ $4 \times 10^{-3} < X(\text{O}) < 5 \times 10^{-3}$
HBBS extreme (20 per cent), C (20 per cent), O (60 per cent)	$8 \times 10^{-3}$	0.1–0.3	3.5–6	0.1–1	Sil. (0.1 $\mu\text{m}$ ) $\text{Al}_2\text{O}_3$ (0.05–0.07 $\mu\text{m}$ )	CNO processed
FS O	$4-8 \times 10^{-3}$	2–10	1–2	0.01–0.1	Sil. (0.07–0.09 $\mu\text{m}$ ) $\text{Al}_2\text{O}_3$ (0.003 $\mu\text{m}$ )	oxygen-rich star
CMS O (10 per cent), C (90 per cent)	$10^{-3}$ (80 per cent) $4-8 \times 10^{-3}$ (30 per cent)	Any	1–6	<0.1	various	various

**Figure 17.** Comparison between the position (grey dots) of the AGBs classified by Riebel et al. (2010) as C-rich (left panel) and O-rich (middle) candidates and extreme stars (right) in the colour-colour  $[3.6] - [4.5]$ ,  $[5.8] - [8.0]$  diagram, compared with the locii defined by OCS, HBBS, FS and CMS stars. In this plane FS are indistinguishable from CMS, thus we show the FS+CMS groups together (in the colour version of this figure, available in the online version, OCS are shown with green points, HBBS with red points, the FS+CMS group with blue points).

as shown in the middle and right panels of Fig. 16, in the CCD2 and CMD80 plane the two groups are fairly separated, the oxygen-rich stars occupying the bluer region and C-rich models defining a redder, parallel sequence. Indeed the tracks of the two groups of models bifurcate in this plane, as shown in the right panels of Fig. 8. The reason for this lies in the strong depression of the 3.6- $\mu\text{m}$  flux that characterizes the C-rich models, which makes the  $[3.6] - [8.0]$  colours redder. Spectroscopic analysis of these stars could further confirm this interpretation.

In Table 3 we present a summary of our interpretation. For each of the four groups into which we divide the LMC AGBs, we give information on the metallicity, epoch of formation, initial masses of the precursors, surface chemical composition and dust present in the circumstellar envelope. We also show (second column) how stars in each group would be sampled according to the original classification by Riebel et al. (2010); we discuss this point in the next section.

## 7 THE INTERPRETATION OF OBSERVED C-RICH, O-RICH CANDIDATES AND EXTREME AGBS IN THE LMC

As explained in Section 5.1, Riebel et al. (2010) proposed a classification of AGB stars based on their *Spitzer* colour and magni-

tudes. The final sample of stars, published in Riebel et al. (2012), is divided among carbon stars (C), oxygen-rich objects (O) and ‘extreme’ stars. The criterion followed to distinguish between C-rich and O-rich objects is based on the scheme by Cioni et al. (2006) and is shown in fig. 1 of Riebel et al. (2012). Extreme AGB candidates were selected based on the  $J - [3.6]$  colour.

We introduced slightly tighter sample selection than Riebel et al. (2010) for quality-control purposes. We further define a new classification scheme, based on theoretically predicted tracks and LMC populations/star-forming history.

We now compare the results from our interpretation with the photometric classification by Riebel et al. (2010, 2012), to check whether our models are in agreement with the division into C and oxygen-rich stars given by these authors and to characterize the sample of objects classified as ‘extreme’ by Riebel et al. (2010).

Table 3 (column 2) illustrates the composition of each of the four AGB groups in terms of the classification by Riebel et al. (2010). For each population, we also give information concerning the formation epoch, the degree of obscuration and the properties of the dust in the wind. Fig. 17 shows the comparison between the position of the AGBs classified by Riebel et al. (2010) as C-rich (left panel), O-rich candidates (middle) and extreme stars (right) in the CCD and the locii defined by OCS green points, HBBS red points, FS and CMS stars. In this plane, FS are indistinguishable from CMS, thus we show the FS+CMS groups together (blue points).

The stars classified as extreme are the  $\sim 20$  per cent of the sample examined here (see right panel of Fig. 17); this group is mainly composed of dust-obscured carbon stars (OCS, 83 per cent), with smaller contributions from CMS ( $\sim 15$  per cent) and oxygen-rich HBBS ( $\sim 2$  per cent). This reinforces the idea that most ( $\sim 95$ – $97$  per cent) of the extreme AGBs are C-star candidates, surrounded by optically thick envelopes.

C stars, shown in the left panel of Fig. 17, are located on the left side of the diagram, in the region  $[3.6] - [4.5] < 0.4$ . In this group we find  $\sim 55$  per cent of the stars of our sample. As expected, the vast majority of C stars fall within the CMS+FS group, shown in blue in Fig. 17. On the evolutionary side, these stars correspond to either C stars with a C/O ratio slightly above unity or objects with a much larger C/O, in the phases following the TP. A few C stars ( $\sim 3$  per cent) were identified in this investigation as OCS and correspond to the grey points in the zone  $0.2 < [3.6] - [4.5] < 0.4$  overlapped with the green dots in the left panel of Fig. 17; this clearly depends on the assumed threshold in the  $[3.6] - [4.5]$  colour used to define the OCS group. A few sources, which according to our interpretation are HBBS, are classified as C stars (31 objects,  $\sim 1$  per cent of the C-star sample). We believe that this is due to the criterion, described in Section 4, used to separate the C stars from the oxygen-rich star sample, based on the position of the individual objects in the colour–magnitude diagram ( $J - K_s$ ,  $K_s$ ) and on the assumption that oxygen-rich stars populate an almost vertical strip, bluer than the C-star sequence (see fig. 1 of Cioni et al. 2006). This definition holds in as far as the stars are not obscured, but neglects migration to the red (hence to the zone occupied by C stars) of the oxygen-rich star tracks once the envelope becomes optically thick (see fig. 1 of Riebel et al. 2012).

Finally, we focus on the O-rich candidates, shown in the middle panel of Fig. 17. 95 per cent of these stars belong to the CMS group and also to the FS stars populating the finger in the ( $[8.0] - [24]$ ,  $[24]$ ) plane. A small fraction, below 2 per cent, comprise part of the HBBS indicated in red in Fig. 17. A few O stars are classified as OCS and correspond to the grey dots overlapped with the green points in the middle panel of Fig. 17: however, these points are very close to the assumed boundary separating OCS from the (FS+CMS) sample, with a difference in magnitude  $\sim 0.1$  mag, well below the photometric error in  $[3.6] - [4.5]$ .

## 8 THE DUST PRODUCTION RATE FROM AGBS IN THE LMC

The determination of the dust production rate (DPR) by AGBs in the LMC is currently a major issue, one it is believed will provide important information on the role of AGB stars in dust enrichment of the ISM.

Different modalities to find the DPR have been adopted so far. The works by Srinivasan et al. (2009) and Boyer et al. (2012) are based on the assumed correlation between the rate at which dust is ejected from the star+envelope system,  $\dot{M}_d$ , and the  $8.0\text{-}\mu\text{m}$  excess; Matsuura et al. (2009) and Matsuura, Woods & Owen (2013) use a relation between the gas mass-loss rate,  $\dot{M}$ , and the IR colours; the approach by Riebel et al. (2012) relies on the fitting of individual SEDs, in turn providing  $\dot{M}_d$ .

Here we find the DPR based on the results of our simulation, giving the mass-loss rate experienced by the stars populating the synthetic diagrams. Note that we do not need any a priori assumption of the gas/dust ratio, as the individual  $\dot{M}_d$  are found by the degree of condensation of the various key species (carbon for C stars, silicon for oxygen-rich stars), which is a result of our modelling (Ventura et al. 2014b).

To determine the dust production rate for each individual object coming from our simulation at a given moment of AGB evolution, we proceed as in Ferrarotti & Gail (2006). Concerning oxygen-rich stars, the dust production rate at a given evolutionary phase is given by the contribution of the dust produced under the form of silicates, corundum and iron:

$$\dot{M}_d = \dot{M}_{\text{sil}} + \dot{M}_{\text{cor}} + \dot{M}_{\text{Fe}},$$

with

$$\dot{M}_{\text{sil}} = \dot{M} X_{\text{Si}} A_{\text{Si}} / A_{\text{Si}} \text{frac}(\text{Si}),$$

$$\dot{M}_{\text{cor}} = \dot{M} X_{\text{Al}} A_{\text{Al}_2\text{O}_3} / A_{\text{Al}} \text{frac}(\text{Al}),$$

$$\dot{M}_{\text{Fe}} = \dot{M} X_{\text{Fe}} \text{frac}(\text{Fe}).$$

Concerning C stars, we consider the contributions from solid carbon, SiC and iron:

$$\dot{M}_d = \dot{M}_C + \dot{M}_{\text{SiC}} + \dot{M}_{\text{Fe}},$$

with

$$\dot{M}_C = \dot{M} X_C \text{frac}(\text{C}),$$

$$\dot{M}_{\text{SiC}} = \dot{M} X_{\text{Si}} A_{\text{SiC}} / A_{\text{Si}} \text{frac}(\text{Si}),$$

$$\dot{M}_{\text{Fe}} = \dot{M} X_{\text{Fe}} \text{frac}(\text{Fe}).$$

In the above expressions, the various ‘frac’ quantities indicate the fraction of the key species condensed into dust;  $X_i$  represents the mass fractions of the key species at the surface of the stars;  $A_i$  indicates the weight of the various species considered.  $\dot{M}_{\text{sil}}$ ,  $\dot{M}_{\text{cor}}$ ,  $\dot{M}_{\text{Fe}}$ ,  $\dot{M}_C$  and  $\dot{M}_{\text{SiC}}$  indicate, respectively, the rate at which silicates, corundum, iron, solid carbon and SiC particles are ejected from the envelope of the star.

In agreement with Schneider et al. (2014), we find an overall DPR of  $\sim 4.5 \times 10^{-5} M_{\odot} \text{ yr}^{-1}$ , with relative contributions from carbon and oxygen-rich stars of, respectively,  $4 \times 10^{-5} M_{\odot} \text{ yr}^{-1}$  and  $5 \times 10^{-6} M_{\odot} \text{ yr}^{-1}$ . Concerning the dust production from oxygen-rich stars, our results indicate that it is almost entirely provided by HBBS, which represent only  $\sim 1$  per cent of the whole AGB sample examined here.

Concerning the carbon component, half of the dust ejection rate is due to stars with  $[3.6] - [4.5] > 1$ , including only  $Z > 4 \times 10^{-3}$  objects.

Compared with the aforementioned investigations, our DPR from C-rich stars is close to the results by Matsuura et al. (2009, 2013), whereas for the O-rich component our findings are in better agreement with Riebel et al. (2012).

## 9 CONCLUSIONS

We use models of stars of intermediate mass ( $1 M_{\odot} \leq M \leq 8 M_{\odot}$ ) evolved through the AGB phase, integrated with the description of the dust formation process in the winds, to interpret *Spitzer* observations of AGBs in the LMC.

We find that the position of the individual sources in the various colour–colour and colour–magnitude diagrams obtained with the *Spitzer* bands is strongly connected to the mass and evolutionary phase experienced by the star; C stars and oxygen-rich objects with dust in their envelopes occupy well-separated zones in some of the observational diagrams. Metallicity is also found to play a role in this context.

Results from our modelling reproduce the observations nicely, in terms of the percentage of stars found in the different regions of the observational planes. The spectroscopically confirmed stars largely confirm our interpretation.

We find that the majority (97 per cent) of the most dust-obscured objects, traditionally classified as ‘extreme’, are carbon stars surrounded by carbonaceous particles. These stars, in the ([3.6] – [4.5], [5.8] – [8.0]) diagram, correspond to the observed diagonal strip at [3.6] – [4.5] > 0.2. Our models suggest that these stars are composed of multiple metallicities, starting from  $Z = 10^{-3}$  to  $Z = 8 \times 10^{-3}$ . Most of them are low-metallicity ( $Z \sim 10^{-3}$ ) objects, with ages ranging from  $4 \times 10^8$  yr to 3 Gyr; however the reddest population, observed at [3.6] – [4.5] > 2, is entirely composed of higher- $Z$  stars ( $Z > 4 \times 10^{-3}$ ) with initial masses  $M \sim 2.5\text{--}3 M_{\odot}$ , in the very latest phases of AGB evolution. They are expected to be surrounded by an internal layer hosting SiC particles of  $\sim 0.08 \mu\text{m}$  size and a more external zone with  $0.15\text{--}0.2 \mu\text{m}$  sized carbon grains.

The remaining part of the extreme sample is composed of more massive objects experiencing HBB, surrounded by alumina dust ( $\sim 0.07 \mu\text{m}$ ) and silicate grains ( $\sim 0.1 \mu\text{m}$ ); these sources are the descendants of stars with initial masses  $M \sim 5\text{--}6 M_{\odot}$  formed  $\sim 10^8$  yr ago. Only metal-rich objects ( $Z \sim 8 \times 10^{-3}$ ) are predicted to populate this subsample.

The overall dust production rate is  $\sim 4.5 \times 10^{-5} M_{\odot} \text{yr}^{-1}$ , with an 85 per cent contribution from C stars, the remaining 15 per cent coming from M stars. The DPR from the latter sample is entirely given by stars experiencing HBB.

The results of this analysis, to be confirmed by further spectroscopic investigations, will allow a considerable step forward in the characterization of the AGB population of the LMC, opening the possibility of interpreting most of the stars observed, particularly those with the strongest dust thermal emission, in terms of the mass of the precursor, metallicity, surface chemistry and the properties of dust present in their winds. The same analysis can be extended to the Small Magellanic Cloud and, thanks to the expected performance of future space missions, to other galaxies of the Local Group.

This study will also have important feedback on the evolution properties of AGBs, particularly towards a better understanding of the two most uncertain physical mechanisms characterizing this evolutionary phase, namely the extent of the third dredge-up and the strength of hot bottom burning experienced by massive AGBs.

## ACKNOWLEDGEMENTS

The authors are indebted to the anonymous referee for a careful reading of the manuscript and for the detailed and relevant comments, which helped to increase the quality of this work. FD and PV are indebted to Simonetta Puccetti for assistance in data selection and handling. DAGH acknowledges support provided by the Spanish Ministry of Economy and Competitiveness under grants AYA201127754 and AYA201129060. PV was supported by PRIN MIUR 2011 ‘The Chemical and Dynamical Evolution of the Milky Way and Local Group Galaxies’ (PI: F. Matteucci), prot. 2010LY5N2T. RS acknowledges funding from the European Research Council under the European Union’s Seventh Framework Programme (FP/2007–2013)/ERC Grant Agreement n. 306476.

## REFERENCES

Aringer B., Girardi L., Nowotny W., Marigo P., Lederer M. T., 2009, *A&A*, 503, 913

- Beelen A., Cox P., Benford D. J., Dowell C. D., Kovacs A., Bertoldi F., Omont A., Carilli C. L., 2006, *ApJ*, 642, 694
- Bertoldi F. et al., 2003, *A&A*, 409, L47
- Bertschinger E., Chevalier R. A., 1985, *ApJ*, 299, 167
- Bianchi S., Schneider R., 2007, *MNRAS*, 378, 973
- Blanco B. M., Blanco V. M., McCarthy M. F., 1978, *Nature*, 271, 638
- Blöcker T., 1995, *A&A*, 297, 727
- Blöcker T., Schönberner D., 1991, *A&A*, 244, L43
- Blum R. D. et al., 2006, *AJ*, 132, 2034
- Bowen G. H., 1988, *ApJ*, 329, 299
- Boyer M. L., 2013, *Astron. Nachr.*, 334, 124
- Boyer M. L. et al., 2011, *AJ*, 142, 103
- Boyer M. L. et al., 2012, *ApJ*, 748, 40
- Calura F., Pipino A., Matteucci F., 2008, *A&A*, 479, 669
- Canuto V. M. C., Mazzitelli I., 1991, *ApJ*, 370, 295
- Carrera R., Gallart C., Hardy E., Aparicio A., Zinn R., 2008, *AJ*, 135, 836
- Cioni M. R. L., Girardi L., Marigo P., Habing H. J., 2006, *A&A*, 448, 77
- Cioni M.-R. L. et al., 2000a, *A&AS*, 144, 235
- Cioni M.-R. L., Habing H. J., Israel F. P., 2000b, *A&A*, 358, L9
- Cloutmann L., Eoll J. G., 1976, *ApJ*, 206, 548
- De Bressan M., Schneider R., Valiante R., Salvadori S., 2014, *MNRAS*, 445, 3039
- Dell’Agli F., 2012, PhD thesis, University of Rome ‘Roma Tre’
- Dell’Agli F., Ventura P., Garcia-Hernandez D. A., Schneider R., Di Criscienzo M., Brocato E., D’Antona F., Rossi C., 2014a, *MNRAS*, 442, L38
- Dell’Agli F., Garcia-Hernandez D. A., Rossi C., Ventura P., Di Criscienzo M., Schneider R., 2014b, *MNRAS*, 441, 1115
- Di Criscienzo M. et al., 2013, *MNRAS*, 433, 313
- Doherty C. L., Gil-Pons P., Lau H. B., Lattanzio J. C., Siess L., Campbell S. W., 2014, *MNRAS*, 441, 582
- Dwek E., 1998, *ApJ*, 501, 643
- Dwek E., Cherchneff I., 2011, *ApJ*, 727, 63
- Epchtein N., Omont A., Burton B., Persi P., 1994, *Ap&SS*, 217, 3
- Feast M., 1999, *PASP*, 111, 775
- Ferrarotti A. D., Gail H. P., 2001, *A&A*, 371, 133
- Ferrarotti A. D., Gail H. P., 2002, *A&A*, 382, 256
- Ferrarotti A. D., Gail H. P., 2006, *A&A*, 553, 576
- Fleischer A. J., Gauger A., Sedlmayr E., 1992, *A&A*, 266, 339
- Freytag B., Ludwig H.-G., Steffen M., 1996, *A&A*, 313, 497
- Frogel J. A., Mould J., Blanco V. M., 1990, *ApJ*, 352, 96
- Gail H. P., Sedlmayr E., 1985, *A&A*, 148, 183
- Gail H. P., Sedlmayr E., 1999, *A&A*, 347, 594
- Grevesse N., Sauval A. J., 1998, *Space Sci. Rev.*, 85, 161
- Gruendl R. A., Chu Y. H., Seale J. P., Matsuura M., Speck A. K., Sloan G. C., Looney L. W., 2008, *ApJ*, 688, L9
- Harris J., Zaritsky D., 2009, *ApJ*, 138, 1243
- Hauschildt P. H., Allard F., Ferguson J., Baron E., Alexander D. R., 1999, *ApJ*, 525, 871
- Herwig F., 2005, *AR&A*, 43, 435
- Jaeger C., Mutschke H., Begemann B., Dorschner J., Henning T., 1994, *A&A*, 292, 641
- Knapp G. R., Morris M., 1985, *ApJ*, 292, 640
- Koike C., Kaito C., Yamamoto T., Shibai H., Kimura S., Suto H., 1995, *Icarus*, 114, 203
- Maiolino R., Schneider R., Oliva E., Bianchi S., Ferrara A., Mannucci F., Pedani M., Roia Sogorb M., 2004, *Nature*, 431, 533
- Marigo P., 2002, *A&A*, 387, 507
- Marigo P., Aringer B., 2009, *A&A*, 508, 1538
- Matsuura M. et al., 2009, *MNRAS*, 396, 918
- Matsuura M., Woods P. V., Owen P. J., 2013, *MNRAS*, 429, 2527
- Mattsson L., 2011, *MNRAS*, 414, 781
- Mazzitelli I., D’Antona F., Ventura P., 1999, *A&A*, 348, 846
- Meixner M. et al., 2006, *AJ*, 132, 2268
- Meixner M. et al., 2010, *A&A*, 518, L71
- Meixner M. et al., 2013, *AJ*, 146, 62
- Morgan M. L., Edmunds M. G., 2003, *MNRAS*, 343, 427

- Nanni A., Bressan A., Marigo P., Girardi L., 2013a, MNRAS, 434, 488
- Nanni A., Bressan A., Marigo P., Girardi L., 2013b, MNRAS, 434, 2390
- Nanni A., Bressan A., Marigo P., Girardi L., 2014, MNRAS, 438, 2328
- Nenkova M., Ivezić Z., Elitzur M., 1999, in Sprague A., Lynch D. K., Sitko M., eds, LPI Contributions 969, Workshop on Thermal Emission Spectroscopy and Analysis of Dust, Disks, and Regoliths. Lunar and Planetary Institute, Houston, TX, p. 20
- Nozawa T., Kozasa T., Habe, 2006, ApJ, 648, 435
- Ordal M. A., Bell R. J., Alexander R. W., Newquist L. A., Query M. R., 1988, Applied Optics, 27, 1203
- Ossenkopf V., Henning T., Mathis J. S., 1992, A&A, 261, 567
- Paczyński B., 1970, Acta Astron., 20, 47
- Pegourie B., 1988, A&A, 194, 335
- Piatti A. E., Geisler G., 2013, AJ, 145, 17
- Pipino A., Fan X. L., Matteucci F., Calura F., Silva L., Granato G., Maiolino R., 2011, A&A, 525, A61
- Priddey R. S., Isaac K. G., McMahon R. G., Richard G., Robson E. I., Pearson C. P., 2003, MNRAS, 334, L74
- Renzini A., Voli M., 1981, A&A, 94, 175
- Richer H. B., Westerlund B. E., 1983, ApJ, 264, 114
- Riebel D., Meixner M., Fraser O., Srinivasan S., Cook K., Vijn U., 2010, ApJ, 723, 1195
- Riebel D., Srinivasan S., Sargent B., Meixner M., 2012, AJ, 753, 71
- Robson I., Priddey R. S., Isaac K. G., McMahon R. G., 2004, MNRAS, 351, L29
- Sackmann I. J., Boothroyd A. I., 1992, ApJ 392, L71
- Sargent B. A., Srinivasan S., Meixner M., 2011, ApJ, 728, 93
- Schlegel D. J., Finkbeiner D. P., Davis M., 1998, ApJ, 500, 525
- Schneider R., Valiante R., Ventura P., Dell’Aglì F., Di Criscienzo M., Hirashita H., Kemper F., 2014, MNRAS, 442, 1440
- Silvia D. W., Smith B. D., Shull J. M., 2010, ApJ, 715, 1575
- Silvia D. W., Smith B. D., Shull J. M., 2012, ApJ, 748, 12
- Skrutskie M., 1998, in Epchtein N., ed., Astrophysics and Space Science Library Vol. 230, The Impact of Near-Infrared Sky Surveys on Galactic and Extragalactic Astronomy, Proc. 3rd Euroconference on Near-Infrared Surveys. Kluwer, Dordrecht, p. 11
- Skrutskie M. F. et al., 2006, AJ, 131, 1163
- Sloan G. C., Kraemer K. E., Wood P. R., Zijlstra A. A., Bernard-Salas J., Devost D., Houck J. R., 2008, ApJ, 686, 1056
- Srinivasan S. et al., 2009, AJ, 137, 4810
- Srinivasan S., Sargent B. A., Meixner M., 2011, A&A, 532, A54
- Valiante R., Schneider R., Bianchi S., Andersen A., Anja C., 2009, MNRAS, 397, 1661
- Valiante R., Schneider R., Salvadori S., Bianchi S., 2011, MNRAS, 416, 1916
- Ventura P., D’Antona F., 2005, A&A, 431, 279
- Ventura P., D’Antona F., 2009, MNRAS, 499, 835
- Ventura P., Marigo P., 2009, MNRAS, 399, L54
- Ventura P., Marigo P., 2010, MNRAS, 408, 2476
- Ventura P., Zeppieri A., Mazzitelli I., D’Antona F., 1998, A&A, 334, 953
- Ventura P., Carini R., D’Antona F., 2011, MNRAS, 415, 3865
- Ventura P. et al., 2012a, MNRAS, 420, 1442
- Ventura P. et al., 2012b, MNRAS, 424, 2345
- Ventura P., Di Criscienzo M., Carini R., D’Antona F., 2013, MNRAS, 431, 3642
- Ventura P., Dell’Aglì F., Di Criscienzo M., Schneider R., Rossi C., La Franca F., Gallerani S., Valiante R., 2014a, MNRAS, 439, 977
- Ventura P., Di Criscienzo M., D’Antona F., Vesperini E., Tailo M., Dell’Aglì F., D’Ercole A., 2014b, MNRAS, 437, 3274
- Wachter A., Schröder K. P., Winters J. M., Arndt T. U., Sedlmayr E., 2002, A&A, 384, 452
- Wachter A., Winters J. M., Schröder K. P., Sedlmayr E., 2008, A&A, 486, 497
- Wang R. et al., 2008, ApJ, 687, 848
- Wang R., Wagg J., Carilli C. L., Walter F., Lentati L., Fan X., Riechers D. A., Bertoldi F., 2013, ApJ, 773, 44
- Weisz D. R., Dolphin A. E., Skillman E. D., Holtzman J., Dalcanton J. J., Cole A. A., Neary K., 2013, MNRAS, 431, 364
- Whitney B. A. et al., 2008, AJ, 136, 18
- Wood P. R., 1979, ApJ, 227, 220
- Woods P. M. et al., 2011, MNRAS, 411, 1597
- Zaritsky D., Harris J., Thompson I. B., Grebel E. K., 2004, AJ, 128, 1606
- Zhukovska S., Henning T., 2013, A&A, 555, 99
- Zhukovska S., Gail H.-P., Trieloff M., 2008, A&A, 479, 453
- Zijlstra A. A. et al., 2006, MNRAS, 370, 1961

This paper has been typeset from a  $\text{\TeX}/\text{\LaTeX}$  file prepared by the author.